

Preprint :

Effect of chemical disequilibrium during metal-silicate partitioning on the thermal state of the early core

By Vincent Clesi^{1,2} and Renaud Deguen^{2,3}

¹. Institut für Mineralogie, Münster Universität, Correnstr. 24, 48149 Münster, NRW, Deutschland

². Univ Lyon, ENSL, UCBL, UJM, CNRS, LGL-TPE, F-69007 Lyon, France

³. Université Grenoble Alpes, Université Savoie Mont-Blanc, CNRS, IRD, Université Gustave Eiffel, ISTERre, 38000 Grenoble France

This a preprint of an article submitted to *Advances in Geochemistry and Cosmochemistry* in March 2026.

This is the third version of the preprint.

This version includes the manuscript and the supplementary data.

1 Effect of chemical disequilibrium during 2 metal-silicate partitioning on the thermal state 3 of the early core

4 Vincent Clesi^{1,2}✉  Renaud Deguen^{2,3} 

5 ¹ Institut für Mineralogie, Münster Universität, Correnstraße 24, 48149 Münster

6 ² Univ Lyon, ENSL, UCBL, UJM, CNRS, LGL-TPE, F-69007 Lyon, France

7 ³ Univ. Grenoble Alpes, Univ. Savoie Mont Blanc, CNRS, IRD, Univ. Gustave Eiffel,
8 ISTERre, 38000 Grenoble, France

9 **Author contributions:** Conceptualization: VC, RD. Formal analysis: VC. Writing – original
10 draft: VC. Writing – review & editing: VC, RD.

11 **Supplementary material:** <https://doi.org/10.5281/zenodo.18940615>

12 Abstract

13 In this study, we improved a previously published numerical model linking the core
14 composition to the core temperature during accretion by introducing the possibility of
15 chemical disequilibrium during the segregation of the core in the magma ocean phase.
16 Our study shows that at least 60% of the accreting metal needs to be equilibrated
17 in order to obtain a chemically coherent Earth, thus favoring a rapid core formation
18 according to the Hf-W chronometer. The dilution factor of this equilibrated metallic
19 mass needs to be 4 (for 100% of metallic mass equilibrated) to 40 (for 60% of
20 the metallic mass equilibrated) in order to obtain concentrations of major and trace
21 element close to the Bulk Silicate Earth composition. At the minimum degree of
22 equilibrium in metal and silicate phases, the final temperature of the core is increased
23 by ~ 250 K compared to the fully equilibrated case. The chemical disequilibrium could
24 be then one factor favoring the hot core hypothesis, but has to be coupled with other
25 phenomena (gravitational energy dissipation, radiogenic heat production) to produce
26 a hot core.

27 1 Introduction

28 The presence of light elements in the core has been demonstrated for a long time
29 (Birch, 1965), and constraining the nature and concentrations of these light elements

30 is important to understand the so-called core density deficit (Dziewonski and Ander-
31 son, 1981). The incorporation of light elements in the core has been proposed to
32 happen in a deep magma ocean, where the core-forming metal segregates from the
33 silicate (e.g. Drake and Righter, 2002; Bouhifd and Jephcoat, 2011). This formation
34 at high pressure and high temperature favors the incorporation of light elements in
35 the core, the main light elements being Si and O (Rubie et al., 2015; Fischer et al.,
36 2017; Clesi and Deguen, 2023; Pu et al., 2025). The final composition of the core,
37 and in particular the concentrations of light elements, is dependent on several factors,
38 the main factors being the composition of the building blocks of the Earth and the
39 P-T- f_{O_2} conditions of metal-silicate segregation in a deep magma ocean. Among
40 those conditions, the efficiency of mixing in the magma ocean and the degree of
41 chemical equilibrium is often overlooked, with a majority of models focusing on the
42 end-member with full equilibrium (e.g. Wood et al., 2008; Siebert et al., 2012; Fischer
43 et al., 2015, 2017; Clesi et al., 2016; Clesi and Deguen, 2023; Loroch et al., 2024; Pu
44 et al., 2025). The effect of disequilibrium is complex to apprehend, as two phases are
45 involved (e.g. Rubie et al., 2003; Ulvrová et al., 2011; Gu et al., 2023) with dynamic
46 separation of the two phases that are complex to model (e.g. Samuel, 2012; Deguen
47 et al., 2014; Landeau et al., 2021) with elemental specific equilibrium rates (Clesi
48 et al., 2020). In a previous work (Clesi and Deguen, 2023), we used an accretion
49 model combining the metal-silicate partitioning behavior of different elements and
50 a thermal evolution model of the metallic phase, dependent on the metallic phase
51 composition, to link the thermal evolution of the core to its composition. This model
52 tends to favor the cold core hypothesis (Nomura et al., 2014; Zhang et al., 2016;
53 Dobrosavljevic et al., 2022), particularly if the amount of gravitational dissipation
54 energy going to the metal is low (Monteux et al., 2009; Samuel et al., 2010). The
55 hot core hypothesis (King and Olson, 2011; Andrault et al., 2017; Driscoll and Davies,
56 2023), to be true, necessitates other mechanisms than the simple compressional
57 heating used in Clesi and Deguen (2023). One factor that could increase the initial
58 core temperature is the chemical disequilibrium during the metal-silicate segregation

59 process. Indeed, to explain the bulk silicate Earth composition while considering
60 chemical disequilibrium during core mantle segregation, it is necessary to increase
61 the average depth of the magma ocean (Rubie et al., 2003, 2011; Gu et al., 2023).
62 Clesi and Deguen (2023) showed that such an increase in average magma ocean
63 depth translates into higher core temperatures as well as higher concentrations of Si
64 and O. Therefore, in this study, we modify the model of Clesi and Deguen (2023)
65 by introducing various degrees of disequilibrium in the metallic and silicate phase
66 during the accretion process. We used the results to quantify the effect of chemical
67 disequilibrium on the initial core temperature. We showed that a minimum 60% of
68 the metallic phase needs to be equilibrated with the silicate; and that introducing
69 some degree of disequilibrium favors the formation of a hotter core at the end of
70 accretion, but not hot enough to comply with the 'hot core' hypothesis.

71 2 Description of the thermal model

72 To determine the heat content and temperature of the core we consider the following
73 steps :

- 74 (i) The initial temperature of each addition of metal to the core is set at the bottom
75 of the magma ocean, where the metal is assumed to equilibrate with the silicates.
76 The initial temperature is therefore given by the liquidus of silicate at the pressure
77 of the bottom of the magma ocean, as given by Andrault et al. (2011).
- 78 (ii) The metal is then heated by compression while migrating from the bottom of the
79 magma ocean to the growing core. At each step of accretion its composition is
80 different, and we do not consider any mixing of the core, thus resulting in the
81 formation of a stratified core (as in Jacobson et al. (2017)).
- 82 (iii) The metal is further heated by compression due to the growth of the core up to
83 its final size. We use the resulting temperature and density profiles to calculate
84 the heat content of the core.

85 (iv) We assume that the core is then mixed from the stratified state, and use the
 86 previously calculated heat content to get the temperature at the CMB (T_{CMB}^{is})
 87 assuming the core to be isentropic. That the core is mixed at the end of accretion
 88 is a somewhat strong assumption (Jacobson et al., 2017), but it has the advantage
 89 of allowing to quantify the thermal state of the core with a single parameter (here
 90 the CMB temperature), which greatly simplifies the analysis.

91 The details on the model and the different calculations are described in Clesi and
 92 Deguen (2023), but we propose a quick description of the thermal model in the
 93 following paragraphs.

94 The initial temperature of the metal is set to be the liquidus temperature of
 95 the silicate (Andrault et al., 2011) at the bottom of the magma ocean where the
 96 chemical equilibrium happens. It is given by:

$$T_{eq} = 1940 \left(\frac{P_{eq}}{29} + 1 \right)^{1/1.9}, \quad (1)$$

97 where P_{eq} and T_{eq} are the equilibrium pressure and temperature at the base of the
 98 magma ocean. The temperature changes in steps (ii) and (iii) are obtained from:

$$\frac{dT}{T} = \frac{\gamma}{K_s} dP, \quad (2)$$

99 where γ and K_s are the Gruneisen parameter and isentropic bulk modulus. We use
 100 the Murnaghan approximation for the bulk modulus,

$$K_s = K_0 + K'P, \quad (3)$$

101 with $K_0 = 128.49$, and $K' = 3.67$, which yields the following equation of state for
 102 the metal:

$$\frac{\rho(P)}{\rho_0} = \left(1 + \frac{K'}{K_0} P \right)^{1/K'}, \quad (4)$$

103 where ρ denotes density. The value of ρ_0 is varying throughout accretion, depending
 104 on the composition of the metal after chemical equilibration (or lack thereof in this

105 study) with the silicates (see [Clesi and Deguen \(2023\)](#) for the details). Following the
 106 study of [Clesi and Deguen \(2023\)](#), we use the formalism of [Al'Tshuler et al. \(1987\)](#)
 107 for the calculation of the Grüneisen parameter γ given by:

$$\gamma = \gamma_{\infty} + (\gamma_0 - \gamma_{\infty}) \left(\frac{\rho_0}{\rho} \right)^{\beta}, \quad (5)$$

108 where $\beta = \gamma_0/(\gamma_0 - \gamma_{\infty})$, with $\gamma_0 = 1.933$ and $\gamma_{\infty} = 0.916$ as refitted in [Clesi and](#)
 109 [Deguen \(2024b\)](#). These values might not be appropriate to get a precise estimate of
 110 the core temperature, but the formalism chosen tends to limit the error introduced by
 111 the uncertainty on γ_0 and γ_{∞} ([Clesi and Deguen, 2024b](#)). Nonetheless, the goal of
 112 the study is not to determine the precise temperature of the core, but to assess the
 113 sensitivity of the thermal model to a specific chemical phenomenon, in this specific
 114 instance the dilution and disequilibrium during core/mantle segregation. With this
 115 Grüneisen formalism, integrating Equation 2 during the accretion yields:

$$T(P) = T_{eq} \left(\frac{K_0 + K'P}{K_0 + K'P_{eq}} \right)^{\frac{\gamma_{\infty}}{K'}} \times \exp \left[\frac{\gamma_0 - \gamma_{\infty}}{\beta} \left(\left(1 + \frac{K'P_{eq}}{K_0} \right)^{-\frac{\beta}{K'}} - \left(1 + \frac{K'P}{K_0} \right)^{-\frac{\beta}{K'}} \right) \right]. \quad (6)$$

116 where P is the final pressure of the metal in the stratified case (the difference between
 117 stratified and mixed core is discussed further in [Clesi and Deguen \(2023\)](#)). The heat
 118 content of the core is then calculated as

$$Q = 4\pi \int_0^{R_{core}} \rho(r) C_p T(r) r^2 dr, \quad (7)$$

119 where R_{core} is the radius of the core, r the distance from the center of the core, and
 120 C_p the specific heat capacity of the metal. The link between the radius of the
 121 core and pressure $P_{core}(r)$ within the core is given by:

$$P_{core}(r) = P_{center} + \left(\frac{P_{CMB} - P_{center}}{R_{core}^2} \right) r^2, \quad (8)$$

122 where P_{center} and P_{CMB} denote pressure at the center of the core and CMB. The
 123 isentropic temperature profile can then be obtained by integrating

$$\left(\frac{\partial \ln T^{is}}{\partial \ln \rho_{core}} \right)_s = \gamma. \quad (9)$$

124 where γ is the Grüneisen parameter given in Equation 5. In the final step of
 125 calculation we consider a fully mixed core with a constant heat content, which allows
 126 us to calculate the temperature at the CMB following:

$$T_{CMB}^{is} = \frac{Q}{4\pi \int_0^{R_c} \rho^{is}(r) C_p T^{is}(r) r^2 dr}, \quad (10)$$

127 which is evaluated numerically. In the following sections, we will evaluate how T_{CMB}^{is}
 128 evolves when applying a chemical disequilibrium at stage (i) of the model, thus
 129 changing the composition and density profile of the core.

130 3 Description of the chemical model

131 The thermal model described above is linked to a chemical model of core/mantle seg-
 132regation. In this section, we present briefly the initial model used in [Clesi and Deguen](#)
 133 [\(2023\)](#), and the modifications made to it so as to model a chemical disequilibrium
 134 during core/mantle segregation.

135 3.1 Inputs of the models

136 We tested a whole range of metal-silicate segregation scenario during accretion. In
 137 all of the models presented below, the initial conditions of core-mantle segregation

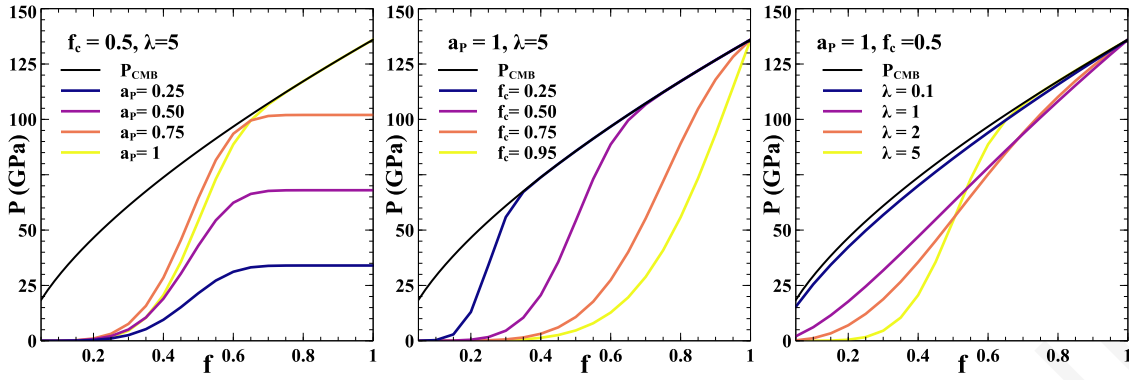


Figure 1: Description of the effect of the parameters used in Equation 11 on the value of P_{eq} . The black line is the pressure at the CMB, $P_{CMB}(f)$. The left panel shows of P_{eq} with $f_c = 0.5$ and $\lambda = 5$ with variable a_P . The middle panel shows the evolution of P_{eq} for $a_P = 1$ and $\lambda = 5$ with variable f_c . The right panel shows the effect of P_{eq} for $a_P = 1$ and $f_c = 0.5$ with λ variable.

138 are fixed by the pressure of equilibrium, representing the bottom of the magma ocean.

139 The pressure of equilibrium, P_{eq} is parameterized by:

$$P_{eq}(f) = a_P P_{CMB}(f) \frac{1 - e^{-(f/f_c)^\lambda}}{1 - e^{-(1/f_c)^\lambda}}, \quad (11)$$

140 where f is the mass fraction of the Earth accreted, $P_{CMB}(f)$ is the pressure at the
 141 CMB for a given mass fraction accreted and the parameters a_P , f_c and λ are the
 142 varying parameters. The average value of P_{eq} , noted $\overline{P_{eq}}$ in the rest of the text, is
 143 representative of the average depth of equilibrium (Clesi and Deguen, 2023), and as
 144 such used preferentially in the interpretations of the results in Section 4.

145 The effect of each parameter on the evolution of the equilibrium pressure P_{eq}
 146 is shown in Figure 1. As shown in the left panel of Figure 1, a_P is the parameter
 147 controlling the maximum pressure at the end of accretion, varying between 0.05 and
 148 1. Depending on the values of f_c and λ , the pressure of equilibrium approaches
 149 $a_P P_{CMB}(f)$ sooner or later during the accretion, but the maximum is set by a_P . For
 150 $a_P = 1$, the value of P_{eq} reaches the same value as the pressure at the CMB, for
 151 $a_P = 0.5$, P_{eq} will always be lower or equal to half of the CMB pressure at any point of
 152 accretion. In the middle panel of Figure 1, we show the effect of the scale parameter
 153 f_c on the evolution of the pressure of equilibrium. This parameter sets the moment
 154 in accretion when the pressure increases faster, especially for high values of λ . It

Elements	Reduced material	Oxidized material
Silicate phase		
SiO ₂	51.41	42.19
MgO	37.5	29.40
Al ₂ O ₃	4.62	3.63
CaO	3.75	2.95
FeO	2.24	21.13
NiO (ppm)	10.1	174
CoO (ppm)	5.1	83
Cr ₂ O ₃ (ppm)	4500	6170
V ₂ O ₃ (ppm)	203	164
Metallic phase		
Fe	91.1	89.07
Ni	5.55	10.0
Co	0.26	0.34
Si	2.4	0.0205
Cr (ppm)	6100	870
V (ppm)	9.24	0.775
O	0.04	0.4
Metallic mass fraction of the impactor		
-	0.313	0.165

Table 1: Impactor composition given in Fischer et al. (2015) supplementary material and used in our model. All units are in wt % except where ppm is specified.

155 is also when we chose to change the oxidation state of the impactor, and therefore
156 the initial composition of metal and silicate accreted, from a reduced composition to
157 an oxidized composition (see below and Table 1). Finally, the right panel of Figure
158 1 shows the effect of the shape parameter λ on P_{eq} , determining the shape of the
159 accretion profile. When $\lambda = 0$, Equation 11 becomes $P_{eq}(f) = a_P P_{CMB}(f)$, i.e.
160 the magma ocean pressure is a fixed fraction of the CMB pressure all along the
161 accretion, as it is classical in several other studies (Wood et al., 2008; Siebert et al.,
162 2012; Bouhifd et al., 2007; Clesi et al., 2016). When $\lambda \rightarrow \infty$, the Equation 11
163 becomes a step function with $P_{eq}(f) = 0$ for $f < f_c$ and $P_{eq}(f) = a_P P_{CMB}(f)$ for
164 $f > f_c$. As can be seen in Figure 1, using a finite value of λ , varying between 0.1 and
165 5 in this study, smoothes out the step function, and the transition from a shallow
166 (i.e. low P_{eq}) to a relatively deep magma ocean (i.e. P_{eq} close to the maximum
167 pressure allowed by a_P value).

168 The scale parameter f_c does not only control the transition of regime for high
169 values of λ , but also the composition of the impacting masses. We chose a simple
170 model with only two different initial compositions: one reduced and one oxidized.
171 The compositions, taken from Fischer et al. (2015), exhibit CI-chondritic elemental
172 ratios (Wasson and Kallemeyn, 1988) in order to match the refractory lithophile
173 element trend in the Bulk Silicate Earth (McDonough and Sun, 1995). For $f < f_c$,
174 the Earth is accreting the reduced composition presented in Table 1, and for $f > f_c$
175 the Earth is accreting the oxidized composition presented in Table 1. Accreting
176 reduced material before oxidized material is consistent with N-body simulations of
177 Solar System formation that tend to accrete inner solar system material material
178 (hotter, more reduced and less rich in volatile elements) first and outer solar system
179 material (cooler, more oxidized and rich in volatile elements) at the end of accretion
180 (Morbidelli et al., 2000; Raymond et al., 2009; Izidoro et al., 2021). The parameters
181 and compositions presented in this section are used in all of the models presented in
182 the following subsections, and a schematics of the physical meaning of the model,
183 derived from Clesi and Deguen (2024a), is given in supplementary Figure S1.

184 3.2 Reference chemical model description

185 The core-mantle segregation model we will take as a reference for this study is based
186 on the work of Fischer et al. (2015), with the link to the thermal model being
187 explained in Clesi and Deguen (2023). A qualitative description of the model is given
188 in Figure 2. The model consists of the following steps of calculations:

- 189 i Initialisation of the calculation: we accrete a planetesimal corresponding to 5
190 % of the Earth mass, and calculate the initial core and mantle composition by
191 equilibrating the entire mass of the metal and silicate at a given pressure. This
192 equate to a single stage model for the first 5% of accretion, which is standard for
193 small bodies (e.g. Grewal et al., 2019, and references therein)
- 194 ii Main accretion process: the Earth is growing by adding impactors of 5% of the
195 Earth size. All of the metal in the impactor mass and only the impactor silicate

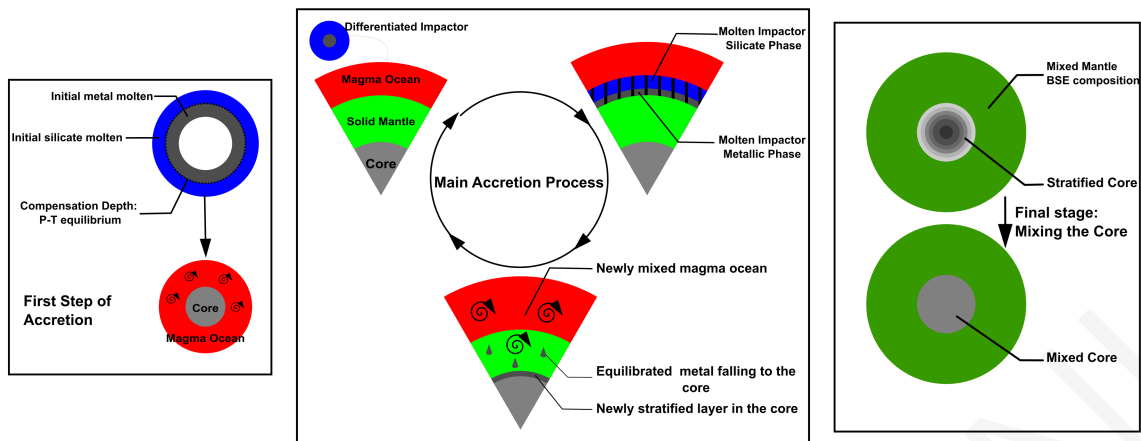


Figure 2: Qualitative description of the model as described in Fischer et al. (2015) and in Section 3.2. The left rectangle described the first step of accretion, setting the initial composition of the planetesimal. The middle rectangle describes the main accretion process: an impactor on a magma ocean is re-equilibrated at the bottom of the magma ocean before segregation of the core and mixing of the whole mantle by vigorous convection. The right rectangle shows the last part of the model: once the mass of the Earth is obtained, we calculate the heat content of a segregated core and calculating the temperature of a mixed core.

196 mass are re-equilibrated at the bottom of the magma ocean, which set the pressure
 197 and temperature of equilibrium (P_{eq} and T_{eq}). The metal then sinks into the core,
 198 adding a chemically different layer on top of the growing core. During the descent,
 199 the temperature of the core is increasing from T_{eq} to its final temperature due to
 200 compressional heating during the migration of the metal through the mantle, and
 201 further compression due to Earth's growth, following Equation 6. It is chemically
 202 insulated from the mantle and the other layers of core. Before another impactor
 203 is added, the mantle is considered well-mixed. This process continues until the
 204 entire Earth mass is accreted.

205 iii Final stage: at the end of the main process, we get a fully accreted Earth with a
 206 stratified core and a well-mixed mantle. We consider that the core is then mixed
 207 isentropically to calculate the temperature at the CMB, T_{CMB}^{is} , given by Equation
 208 10.

209 At each step, the composition of mantle and core is simplified, and we consider the
 210 following equilibrium described by Rubie et al. (2011):

225 12 using the same method. The main calculation consist in solving the mass balance
 226 system of equations:

$$\begin{aligned}
 x + a &= x' + a' \\
 y + b &= y' + b' \\
 z + d &= z' + d' \\
 x + y + 2z + u + m + p + c &= x' + y' + 2z' + u + m + p + c'
 \end{aligned}
 \tag{16}$$

227 with $a, b, c, d, u, m, p, x, y, z, a', b', c', d', x', y', z'$ the number of moles of the
 228 elements involved in reaction 13. This system of equation is combined with the one
 229 created by the K_d of Ni, Si and O, with Equation 15 applied for each element. For
 230 instance for Ni, an element with a valence of 2, expressing Equation 15 becomes:

$$K_d^{Ni} = \frac{b'}{a' + b' + c' + d'} \times \frac{x' + y' + z' + u + m + p}{y'} \times \left(\frac{x'}{x' + y' + z' + u + m + p} \times \frac{a' + b' + d'}{a'} \right)^{2/2}
 \tag{17}$$

231 Combining system 16 with 17 for Ni, Si and O yields a system of 7 equations with
 232 7 unknown ($a', b', c', d', x', y', z'$) that allows for several solutions, only one
 233 respecting the constraint that no mass can be negative. The complexity comes
 234 from the formula of K_d^O , which is calculated using the formula given in [Frost et al.](#)
 235 [\(2010\)](#). The valence 3+ elements (V and Cr) are solved after the main calculation,
 236 because the system would become harder to solve analytically. It introduces an error
 237 in the masses of silicate and metal, but it is limited to a variation of 0.01 to 0.1 %.
 238 The detailed method of solving the system of equation calculation is described in the
 239 supplementary information of [Rubie et al. \(2011\)](#) and [Clesi and Deguen \(2023\)](#). The
 240 number of moles involved in the initial stage of the reaction is calculated using the
 241 mass and composition of the silicate and metal involved in the metal-silicate reaction
 242 12. In the case of the reference model of this study ([Fischer et al., 2015](#); [Clesi and](#)
 243 [Deguen, 2023](#)), the mass of both silicate and metallic phase involved is equal to
 244 the silicate and metal in the impactor (Figure 2). The composition of each phase

involved is also the composition of the impactors, given in Table 1. The number of mole for element in the metal M is therefore:

$$\mathcal{N}_M^{met} = \frac{m_{metal}^{impactor} X_M^{m,imp}}{\mathcal{M}_M}, \quad (18)$$

where \mathcal{N}_M^{met} is the number of mole of M (a,b,c or d in Reaction 12), $m_{metal}^{impactor}$ is the mass of metal in the impactor, $X_M^{m,imp}$ the mass fraction of element M in the metallic phase of the impactor and \mathcal{M}_M the molar mass of element M. As for the silicate, the number of mole of an oxide $MO_{n/2}$ is given by:

$$\mathcal{N}_{MO_{n/2}}^{sil} = \frac{m_{silicate}^{impactor} w_{MO_{n/2}}^{sil,imp}}{\mathcal{M}_{MO_{n/2}}}, \quad (19)$$

with $\mathcal{N}_{MO_{n/2}}^{sil}$ the number of mole of $MO_{n/2}$ (x, y, z, u, m, p in Reaction 12), $m_{silicate}^{impactor}$ the mass of silicate in the impactor, $w_{MO_{n/2}}^{sil,imp}$ the mass fraction of $MO_{n/2}$ in the silicate phase of the impactor and $\mathcal{M}_{MO_{n/2}}$ the molar mass of oxide $MO_{n/2}$.

Since only the impactors are equilibrated, the bulk composition at a given mass fraction is given by:

$$w_{i,bulk}^{s+}(f) = \frac{w_i^s(f) m_{accreted}^s(f) + w_{i,bulk}^{s-} M_{mantle}^-}{M_{mantle}^+}, \quad (20)$$

where $w_{i,bulk}^{s-}(f)$ and $w_{i,bulk}^{s+}(f)$ are the bulk concentrations (in % wt) before and after each addition of mass, and M_{mantle}^- and M_{mantle}^+ the masses of the mantle before and after the impact ($M_{mantle}^+ = M_{mantle}^- + m_{accreted}^s(f)$). When properly calculated at each step of accretion then for $f=1$, Equation 20 yields the bulk composition of the mantle. The same equation can be applied to the core, only by replacing the masses of silicate and mantle by the masses of metal and core respectively.

3.3 Modeling of disequilibrium

Now that the reference model is described, we used the calculation technique of Deguen et al. (2014) to model the disequilibrium between the phases. Since the

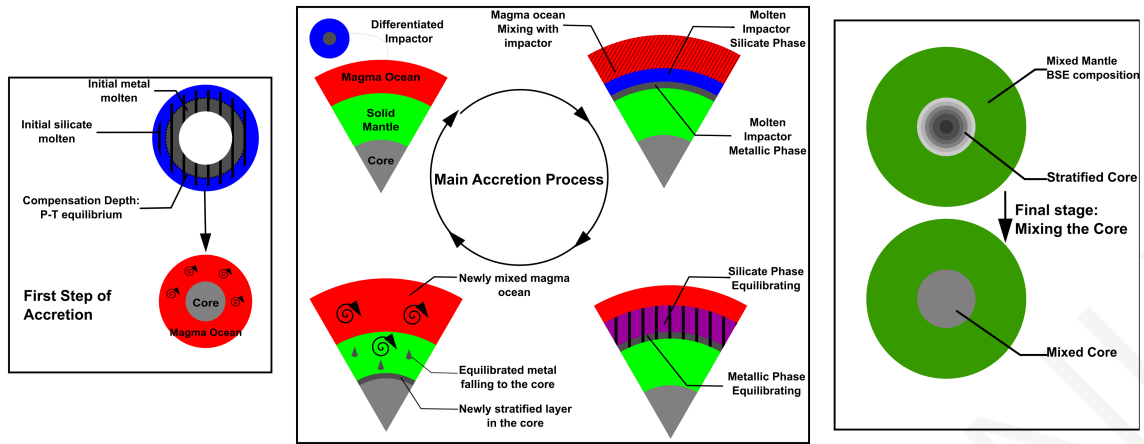


Figure 3: Schematic of the model of disequilibrium used in this study. In all steps only a part of the metal and the silicate is considered to have reacted, even at the first initiation stage. The vertical striped areas represent the amount of metal and silicate reacting. For readability, we considered $k = 1$ (all metal reacted) and an arbitrary value of Δ . Compared to Figure 2, a mixing step has been added before the actual reaction. The amount of silicate equilibrated is colored purple with black stripe in the main accretion stages, and is calculated on the fully mixed magma ocean before reacting with the metal. Once the purple part composition is changed, the magma ocean is fully mixed before the subsequent impact. The last part of the model (re-mixing of the core and mantle) is the same as in the reference model.

265 model is not a time-resolved model, the degree of equilibrium is approximated by the
 266 amount of reacting silicate and reacting metal that are equilibrated. To simplify the
 267 calculation of these masses at each step, we considered that the silicate impactor is
 268 mixed with the previous mantle before reacting.

269 We therefore define, following Deguen et al. (2014), two parameters that are used
 270 to model this phenomenon: k , a parameter describing the amount of metal that is
 271 equilibrated and Δ , the degree of dilution of the metal, i.e. the amount of silicate
 272 that is equilibrated. The parameter k is defined by:

$$k = \frac{m_{eq}^{met}}{m_{total}^{met}}; \quad (21)$$

273 where m_{eq}^{met} is the mass of metal that is equilibrated, and m_{total}^{met} is the total mass of
 274 the metal added from the impactor. The parameter Δ is defined by :

$$\Delta = \frac{m_{eq}^{sil}}{m_{eq}^{met}}; \quad (22)$$

275 where m_{eq}^{sil} is the amount of silicate equilibrated, and m_{eq}^{met} is the amount of metal
 276 equilibrated given by equation 21. This way of defining the degree of equilibrium
 277 links the amount of equilibrium in the silicate to the amount of equilibrium in the
 278 metallic phase, therefore not treating the equilibrium in each phase as independent
 279 parameters. Therefore, direct comparison with studies such as Gu et al. (2023)
 280 cannot be performed as the amount of silicate equilibrated for a given value of Δ
 281 varies first with the value of k (see Equation 22) and varies also within the accretion
 282 model (in particular the parameter f_c , see Figure S.3), since the total amount of
 283 metal added depends on the moment of accretion, the mass added being lower for
 284 the oxidized part of the accretion process (see Section 3.1). For the higher values of
 285 Δ (~ 90 to 100 , depending on the value of k), the entire mantle is equilibrated (see
 286 Figure S.3 for the actual percentage of mantle equilibrated). We tested the models
 287 for k ranging between 0.05 and 1 , and for Δ ranging between 1 and 500 . The values
 288 higher than $\Delta = 100$ are redundant since 99.9 to 100% of the mantle is equilibrated,
 289 but serves as control of the stability of the model.

290 3.4 Definition of a solution and reference model

291 As in Clesi and Deguen (2023), we ran 20 000 models of accretions for each (k, Δ)
 292 couple. In these 20 000 models, the outputs mantle compositions are not necessary
 293 close to the Bulk Silicate Earth (BSE) composition. Therefore, we consider a model
 294 given by a (a_P, f_c, λ) triplet to be a solution if all the elemental concentrations are
 295 within an acceptable range relatively to the BSE as defined in McDonough and Sun
 296 (1995). All major elements concentrations are considered solutions if their values
 297 are within a 10% range of the values of the BSE: $w_{SiO_2}^{mantle} = 45.18 \pm 4.52\%$ wt,
 298 $w_{Al_2O_3}^{mantle} = 4.47 \pm 0.45\%$ wt, $w_{FeO}^{mantle} = 8.10 \pm 0.81\%$ wt, $w_{MgO}^{mantle} = 38.03 \pm 3.80\%$ wt
 299 and $w_{CaO}^{mantle} = 3.56 \pm 0.36\%$ wt. For the trace elements, the concentrations are
 300 considered solutions if their values are within 15% of the values of the BSE: $w_{NiO}^{mantle} =$
 301 2509 ± 376 ppm, $w_{CoO}^{mantle} = 134 \pm 20$ ppm, $w_{V_2O_3}^{mantle} = 121 \pm 18$ ppm and $w_{Cr_2O_3}^{mantle} =$
 302 3859 ± 579 ppm. In this work, the reference model solutions to which everything

will be compared is the model described in Section 3.2 and Figure 2 for which the filter described above has been applied. This differs from Clesi and Deguen (2023) in which we used a weighted method that tends to yield more solutions by allowing some elements concentrations, in particular V and Cr, to be outside the 15% range of the BSE concentration. Overall, the trends highlighted in Clesi and Deguen (2023) (correlation between light elements concentration in the core, core temperature and mean pressure of equilibrium) are the same, with less points (see Figure S.2). Some of the models with high values of $\overline{P_{eq}}$, and therefore higher concentrations of Si and O in the core, are removed from the dataset. A comparison between the solution from Clesi and Deguen (2023) and the reference we use in this study (also used in Clesi and Deguen, 2024a, under the name C20) is presented in Figure S2. This shows that the kind of filter applied to define a solution does affect to some extent the output of the models. Several other filters could have been used for instance using the mean quadratic difference like in Rubie et al. (2015) or using uniquely the N-body simulation results combined with a sensitivity study as in Gu et al. (2023). In any case, the trends we highlighted in Clesi and Deguen (2023) would yield correlations in the same order of magnitude, as evidenced by the comparison of two methods for selecting a solution provided in Figure S2. For the purpose of this study, this issue will not be discussed further, since we will focus on the effect of disequilibrium with a consistent way of selecting the solutions throughout the entire study.

4 Results of the calculations and their implications

4.1 Number of solutions and implications for the Hf-W chronometer

For the range of k and Δ tested, the models yield between 0 and 241 solutions. As shown in Figure 4, most of the disequilibrium models do not yield any solution: for any value of k below 0.6 and for any value of Δ below 4, no model will yield a BSE-like mantle. This shows the need to have at least some equilibration in both phases. For dilution factors Δ superior to 100, the number of solutions for a given

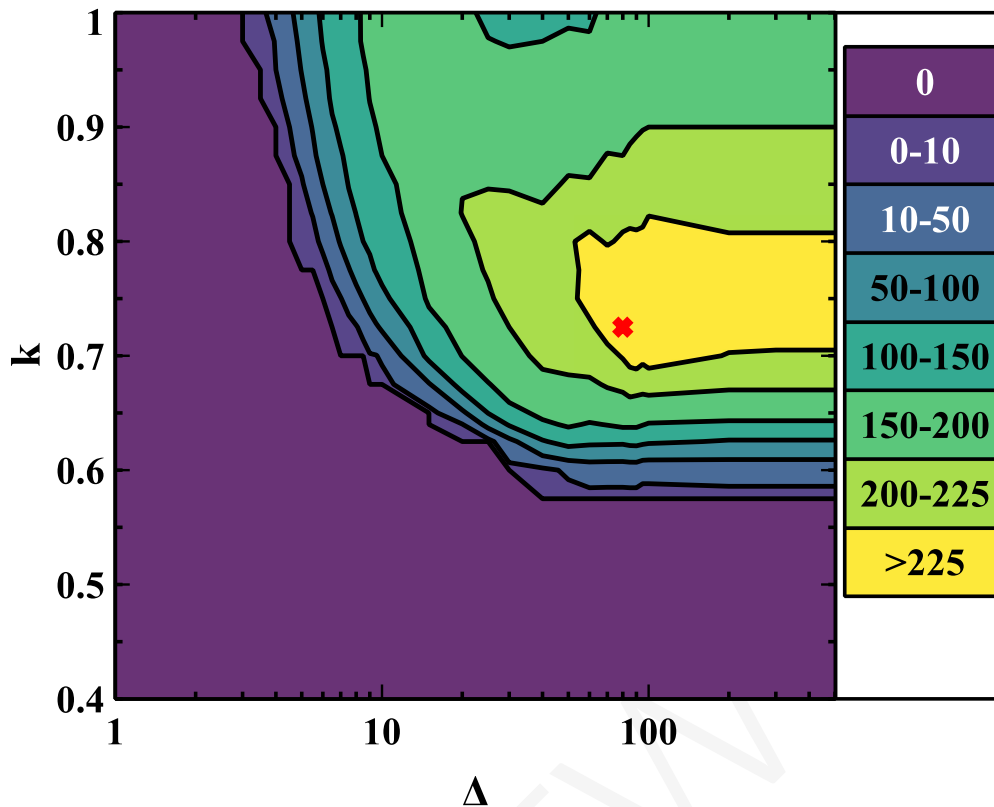


Figure 4: Number of solutions yielded by the model for different values of k (fraction of metal equilibrated, Eq. 21) and Δ (silicate mass equilibrated, see Eq 22). x-axis is in logarithm scale, y-axis in linear scale. The red cross marks the maximum value ($n = 241$) at $k = 0.725$ and $\Delta = 80$.

330 value of k does not change, indicating that the full mantle is equilibrated during the
 331 entire time of accretion (see also Figure S.3). Figure 4 also shows that the maximum
 332 number of solutions is not reached for full equilibration of both phases: the optimum
 333 is obtained when 70 to 80 % of the metallic mass is equilibrated with a dilution
 334 factor between 55 and 100. Higher equilibrium degrees in the metal or in the silicate
 335 do not increase the number of solutions, and even tend to decrease the number of
 336 solutions in the case of the values of k . This indicates that it is easier to model the
 337 accretion of the BSE with some moderate disequilibrium in the metal, at least with
 338 the chondritic material we used in these models. Finally, the number of solutions
 339 drastically decreases for $k < 0.7$ and for $\Delta < 30$. Therefore, while it is easier to
 340 produce a BSE mantle with moderate disequilibrium, it is highly improbable to form
 341 the Earth with a low degree of equilibrium in the silicate or metallic phase.

342 The results laid out in Figure 4 shows that the minimum amount of equilibrium
343 is 60%, higher than the model of Rudge et al. (2010) who proposed a minimum
344 value of 36 %. This could be explained easily by the fact that our parameterization
345 of metal/silicate partitioning is the same as Fischer et al. (2015), while Rudge
346 et al. (2010) used Wood et al. (2008) and Wade and Wood (2005) for moderately
347 siderophile elements. Furthermore, their initial starting material is also different than
348 the one used in the present study, and because disequilibrium is an extensive phenom-
349 ena, even using the same parameterization of metal-silicate partitioning would yield
350 different results. The lowest value of Δ that yields a consistent BSE composition is
351 found to be smaller than found from Deguen et al. (2014): for $k = 1$ we find the
352 minimum value of Δ to be 4, while they propose $\Delta = 17$. This value of 17 is obtained
353 in Deguen et al. (2014) by focusing on the tungsten (W) partitioning in the case of
354 a small magma ocean relatively to the size of the metallic impactor's core.

355 We can further note two things:

- 356 • Our limited number of elements for which we calculate the Earth's composition
357 might not be selective enough to constrain the degree of equilibrium, and adding
358 other elements (among them W or S, for instance) would change the domain of
359 possibility presented in Figure 4
- 360 • Applying a constant value of k and Δ throughout the entire process of accretion is
361 a rough estimation of the degree of disequilibrium, and more precise results would
362 be achieved by including dynamical element to the model (relative size of metallic
363 particles, entrainment coefficient in particular, see Deguen et al. (2014)).

364 In summary, the most probable values of k for our model is comprised between
365 0.7 and 0.8, which, according to the Hf-W chronometer developed by Rudge et al.
366 (2010) will favors rapid formation of the core: between 20 and 50 Myrs (for two-
367 stage or exponential model of accretion, respectively). Further developments of the
368 model need to include more elements, including W, and to take into account the
369 dynamical element of metal-silicate segregation so as to further constrain the time
370 scale of core formation with the degree of equilibrium of metal and silicate.

371 4.2 Chemical equilibrium control on the accretion scenarios

372 In this section we present how the degree of equilibrium affects the type of model
373 that can yield coherent chemical solutions.

374 4.2.1 Effect of silicate dilution

375 On Figure 5 are presented the evolutions of the different input parameter values that
376 yield chemically coherent solutions as a function of the amount of equilibrium in the
377 silicate (Δ) for $k = 0.6$, $k = 0.75$ and $k = 1$. Other plots, in the same fashion
378 but for the other elements composing the mantle and the core, are presented in
379 supplementary Figures S4 to S19. No effect of silicate dilution can be seen on the
380 parameter f_c , which controls the redox state of the impactor: the f_c range is between
381 0.8 and 1, with mean values close to 0.75 for every model, including the reference
382 model. Therefore, the amount of disequilibrium during core-mantle segregation does
383 not affect the redox state significantly: most of the accretion has to be from reduced
384 impactors (more than 80 %) with the more oxidized impactors arriving at the end.
385 For most of the values of Δ , some models can yield chemically coherent Earth mantles
386 for a fully reduced accretion. However, it is impossible to accrete chemically coherent
387 Earth for a fully reduced accretion at very low values of Δ ($\Delta \sim 4 - 7$, Figure 5,
388 panels h. and i.). This effect is enhanced for low values of k (Figure 5, panel g.),
389 which indicates it is impossible not to accrete oxidized material if the degrees of
390 equilibrium in both phases are very low. This effect is common to Δ and k and is
391 discussed further in the following subsection.

392 The effect of silicate disequilibrium on the type of solution obtained is the same
393 for each value of k : as Δ is lowered, the mean pressure of equilibrium during accretion
394 is increased in order to get chemically coherent solutions. This effect is more visible
395 on panels b. and c. of Figure 5: for $k = 0.75$ and $\Delta = 100$, the mean value of $\overline{P_{eq}}$
396 is 18 GPa, while for $\Delta = 7$ the mean value of $\overline{P_{eq}}$ is 28 GPa; and for $k = 1$ the
397 mean value of $\overline{P_{eq}}$ varies between 33 GPa and 18 GPa for Δ varying from 4 to 100,
398 respectively.

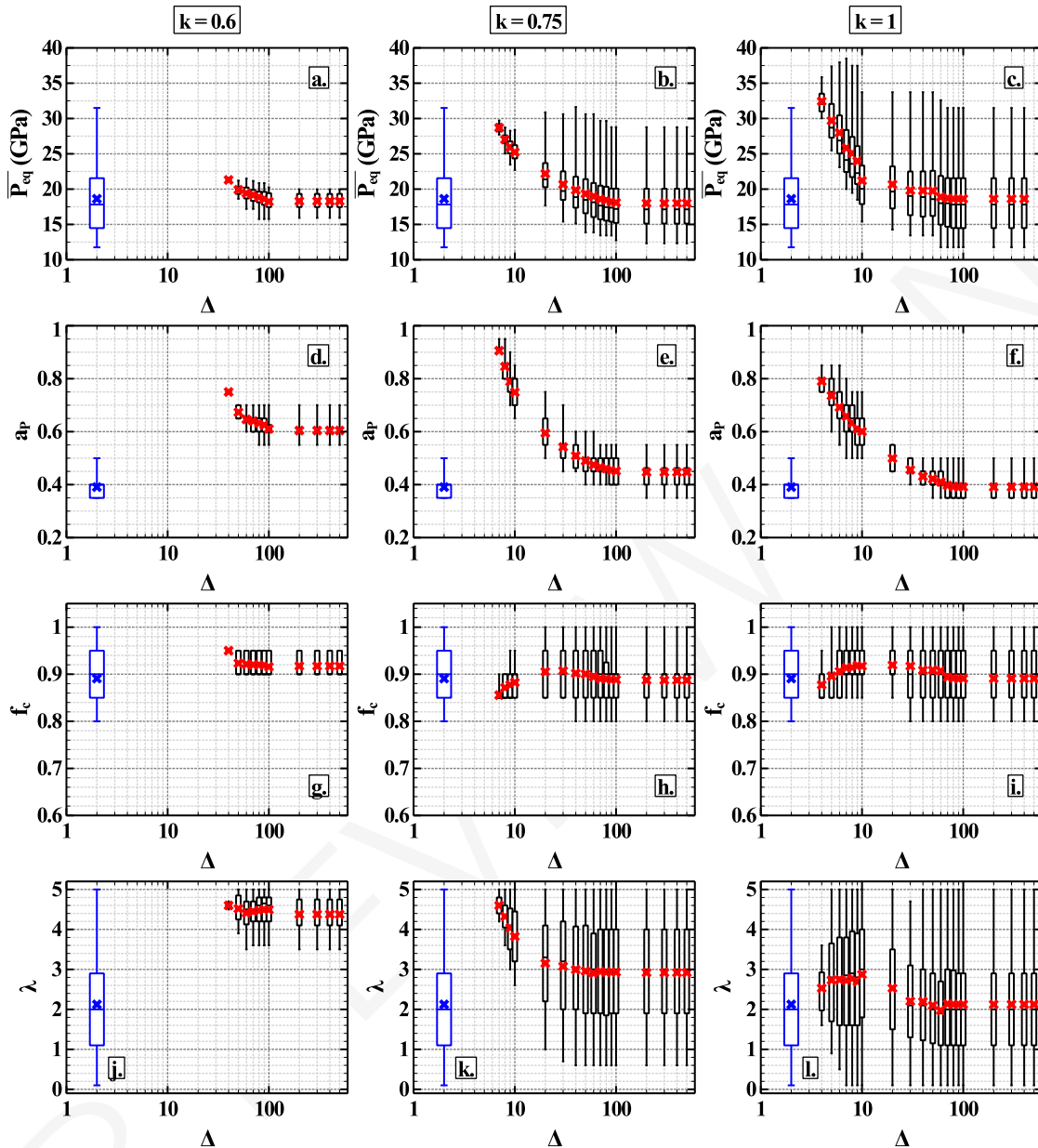


Figure 5: Effect of the silicate dilution Δ on the input parameters controlling the output composition of the model mantle for different values of k . First row, panels a. to c.: $\overline{P_{eq}}$ in GPa. Second row, panels d. to f.: a_p . Third row, panels g. to i.: f_c . Fourth row, panels j. to m.: λ . The left, middle and right column shows the evolution of the parameters values for $k = 0.6$, $k = 0.75$ and $k = 1$, respectively. In each panel the entire solutions range are presented as boxplots, with the red cross being the mean value of the parameter, the white box delimiting the 1st and 3rd quartile, the horizontal line the median value and the vertical lines the minimum and maximum values. The reference model dataset is presented in blue with the same type of plot for comparison, in an arbitrary position for readability.

399 The parameter a_P , which controls the maximum extent of the magma ocean is
400 likewise increased as Δ decreases: for $k = 1$, the mean value of a_P increases from
401 0.4 to 0.8 for Δ decreasing from 100 to 4. This mean that when the degree of
402 equilibrium is low, the magma ocean is twice as deep as when the entire magma
403 ocean is equilibrated, thus leading to higher mean pressure of equilibrium during
404 accretion.

405 The parameter λ , which controls the style of accretion (stable depth of the
406 magma ocean relatively to the size of the planet or sharp transition from shallow to
407 deep magma ocean) is also affected by the silicate dilution imposed on the model. As
408 shown in panels j., k. and l. of Figure 5, the reference model spans the entire range
409 of λ values tested, while it is not the case for the disequilibrated model, especially
410 at low values of k and low values of Δ . Indeed, for $k = 0.75$ the mean value of λ
411 decreases from 4.9 to 3.1 for Δ increasing from 7 to 100. Furthermore, the range
412 of λ values that provides chemically coherent solutions gets narrower as the amount
413 of silicate equilibrated decreases: for $k = 0.6$, the range of λ values is comprised
414 between 3.5 and 5 for all Δ values that yield solutions; for $k = 0.75$, the range varies
415 from 4.2 to 5 for $\Delta = 7$ and from 0.2 to 5 for $\Delta = 100$; and for $k = 1$ the range
416 varies from 1.8 to 3.6 for $\Delta = 4$ and between 0.1 and 5 for $\Delta = 100$. This indicates
417 that when the silicate is not fully equilibrated, the only scenarios of accretion that
418 can yield chemically coherent Earth analogs are the ones that tend to have very
419 shallow magma oceans during most of their accretion process followed by a dramatic
420 increase of magma ocean depth toward the end of accretion.

421 4.2.2 *Effect of metal equilibrium*

422 In Figure 6 are shown the evolutions of input parameters values as functions of the
423 metal degree of equilibrium k for $\Delta = 10$, $\Delta = 50$ and $\Delta = 100$. Other plots,
424 focusing on the other elements composing the core and mantle, are presented in
425 supplementary Figures S4 to S19.

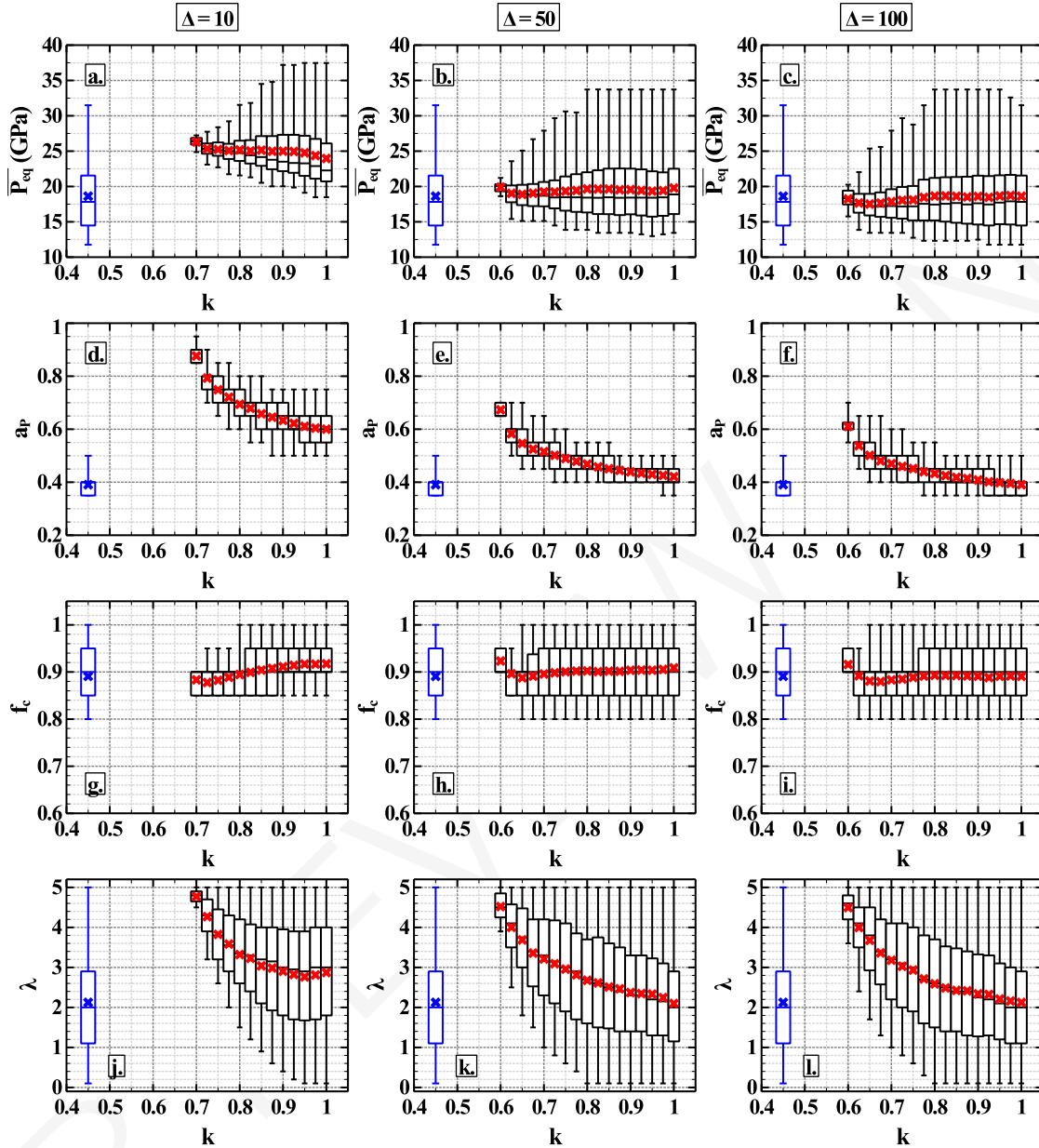


Figure 6: Effect of metal equilibrium k on the input parameters controlling the output composition of the model mantle for different values of Δ . First row, panels a. to c.: $\overline{P_{eq}}$ in GPa. Second row, panels d. to f.: a_p . Third row, panels g. to i.: f_c . Fourth row, panels j. to l.: λ . The left, middle and right column shows the evolution of the parameters values for $\Delta = 10$, $\Delta = 50$ and $\Delta = 100$, respectively. In each panel the entire solutions range are presented as boxplots, with the red cross being the mean value of the parameter, the white box delimiting the 1st and 3rd quartile, the horizontal line the median value and the vertical lines the minimum and maximum values. The reference model dataset is presented in blue with the same type of plot for comparison, in an arbitrary position for readability..

426 Like the silicate dilution effect, the disequilibrium of the metallic phase has little
427 effect on the acceptable f_c values, with all ranges of solution between 0.8 and 1,
428 and mean values of f_c around 0.88 for all values of Δ . This confirms that in order
429 to get chemically consistent Earth's mantles, accretion scenarios need to include at
430 least 80% of reduced material and less than 20 % of oxidized material at the end
431 of accretion, with some solutions possible for 0% of oxidized accreted material. A
432 noticeable trend on the value of this parameter is that as the values of k and Δ get
433 lower, the range of f_c values gets narrower. For the lowest values of k and Δ that
434 yields solutions, no solution can be found for 100% reduced accretion. This effect is
435 only valid for the minimum values of k (between 0.6 and 0.7 depending on Δ) and
436 the minimum values of Δ (4 to 7 depending on the value of k). This indicate that
437 very low degree of equilibrium during accretion render the accretion of some oxidized
438 material necessary in order to obtain a chemically coherent Earth.

439 The parameter k affects the value of λ in the same way as Δ : decreasing the
440 degree of equilibrium tends to select higher values of λ in order to get a solution.
441 For instance, for $\Delta = 50$ (Figure 6, panel k.), the range of λ that yield solutions is
442 comprised between 3.9 and 5 (mean at 4.5) for $k = 0.6$, and is comprised between
443 0.1 and 5, *i.e.* the entire range of λ values tested, for $k = 1$. This shows that
444 decreasing the amount of metal equilibrated during accretion favors models where
445 the magma ocean is shallow at first, turning into a deep magma ocean dramatically
446 at the end of accretion. More metal and silicate equilibration tends to favor on the
447 other hand a more steady increase in the magma ocean depth.

448 The effect of k on $\overline{P_{eq}}$ and a_P is comparable to the effect of Δ : as the amount of
449 metal equilibrated is lowered, the mean pressure of equilibrium is increased in order
450 to get a chemically coherent Earth. This effect is enhanced by lowering the value
451 of Δ : for $\Delta = 100$ (Figure 6, panel f.), the mean value of a_P decreases from 0.61
452 to 0.4 when k increases from 0.6 to 1; for $\Delta = 10$ (Figure 6, panel d.), the mean
453 value of a_P decreases from 0.83 to 0.6 when k increases from 0.7 to 1. This effect
454 is comparable to the effect Δ has on a_P . This shows that the maximum extent of

455 the magma ocean at the end of accretion is significantly affected by the degree of
456 equilibrium both in the silicate and metallic phases. However, the clear effect of Δ on
457 the mean pressure of equilibrium during accretion $\overline{P_{eq}}$, shown in the previous section,
458 is less visible, though still present, when plotting the values of $\overline{P_{eq}}$ as a function of k .
459 Indeed, lower k values tend to yield higher mean values (and mostly median values)
460 of $\overline{P_{eq}}$ than higher values of k : for instance for $\Delta = 10$ (Figure 6, panel a., the
461 mean value of $\overline{P_{eq}}$ is 26 GPa for $k = 0.7$ and $\overline{P_{eq}} = 24$ GPa (the median value being
462 22 GPa) for $k = 1$. This effect is not as clear as the effect of k on a_P , because
463 increasing k tends to widen the range of $\overline{P_{eq}}$, in particular because the maximum
464 value of $\overline{P_{eq}}$ increases with increasing k . For instance, for $\Delta = 100$ (Figure 6, panel
465 c.), the maximum value of $\overline{P_{eq}}$ increases from 20 GPa for $k = 0.6$ to 32.6 GPa for
466 $k = 1$ and reaching a maximum at 33.75 GPa for k between 0.7 and 0.95. This
467 discrepancy in the effect of k on a_P and $\overline{P_{eq}}$ which are highly correlated shows that
468 the degree of metal equilibrium controls more the maximum extent of the magma
469 ocean at the end of accretion (which is the physical meaning of the a_P parameter,
470 Figure S1) than the overall pressure necessary to get a chemically coherent mantle,
471 which is more controlled by the degree of equilibrium in the silicate.

472 4.3 Chemical equilibrium effect on temperature and core composition

473 In this section we present how the degree of equilibrium affects the temperature and
474 composition of the Earth's core.

475 4.3.1 Effect of silicate dilution

476 The main output of our model is the composition of the core, in particular the Si
477 and O contents, and the heat content (T_{CMB}^{is}) it correlates with. In Figure 7 are
478 presented the evolution of this three properties of the core as a function of Δ for
479 $k = 0.6$, $k = 0.75$ and $k = 1$. The more silicate phase equilibrated, the lower the
480 heat content of the core, especially if a large portion of the metal is equilibrated (see
481 panels a. and c. on Figure 7). For instance, when $k = 1$ (panel c., Figure 7), the
482 mean value of T_{CMB}^{is} decreases from 4050 K to 3970 K when Δ increases from 4 to

483 100. This relates to the effect Δ has on the input parameters: the more the silicate
484 is equilibrated, the lower \overline{P}_{eq} needs to be to yield a chemically coherent mantle, and
485 therefore the temperature of the metal accreted to the core is lower. However, this
486 effect on mean values is low, with a decrease of only 100 K for $k = 1$, and 50
487 K for $k = 0.6$, between the minimum equilibrium possible and a full magma ocean
488 equilibration. The effect of k , i.e. metal equilibrium, seems to be more important
489 on the heat content and core temperature (see the range of T_{CMB}^{is} on panels a., b.
490 and c. of Figure 7), which is more discussed in the following section.

491 Because lowering Δ tends to increase \overline{P}_{eq} during accretion, the output core com-
492 positions tend to integrate more light elements as the degree of silicate equilibrium
493 decreases. This is true for both Si and O, with the effect being more important for
494 O than Si. Indeed, the mean values of w_{Si}^{core} for $k = 1$ decreases from 4.8 % wt to
495 3.9 % wt when Δ increases from 4 to 100 (Figure 7, panel f.); while the mean values
496 of w_O^{core} for $k = 1$ (Figure 7, panel i.) decreases from 1.47 to 0.27 % wt when Δ
497 increases from 4 to 100. This shows that the oxygen content of the core is more
498 affected by the mean pressure and type of accretion (higher values of \overline{P}_{eq} , a_P and λ
499 for lower Δ , see Figure 5) than Si, despite both reacting the same way to the lack of
500 equilibrium in the silicate phase. Overall, these results show that there is a positive
501 correlation between the heat content and the light elements concentrations in the
502 core that is mediated by the mean pressure of equilibrium during the metal/silicate
503 segregation phase. The mean pressure of equilibrium is inversely proportional to the
504 silicate equilibrium, and therefore decreasing the amount of silicate equilibrated tends
505 to increase both the heat content and light elements content of the core.

506 4.3.2 *Effect of metal equilibrium*

507 The effect of metal equilibrium k on T_{CMB}^{is} , w_{Si}^{core} and w_O^{core} for fixed values of Δ
508 (10, 50 and 100) is presented in Figure 8. This figure shows that all the output of
509 the model are less sensitive to the amount of metal equilibrated than the amount of
510 silicate equilibrated (see Figure 7 for comparison). The trends in Figure 8, especially

511 on the mean and median values, are not as clear as the trends that emerges when
512 plotting the same parameter as a function of Δ . However, one can note that for
513 $\Delta = 10$, increasing k from 0.7 to 1 lead to a decrease of the mean value of $w_{\text{O}}^{\text{core}}$
514 from 0.97 to 0.65 % wt (Figure 8, panel g.). This decrease is less important than
515 the one observed when varying Δ for $k = 1$ (Figure 7, panel j.), thus indicating a
516 lower sensitivity of Earth's core oxygen content to the metallic equilibrium than to
517 the silicate equilibrium.

518 Most of the effect of k lies mostly in the range of possible output: as more metal
519 equilibrates, it is possible to obtain different core compositions and heat contents and
520 still be chemically coherent with the BSE. Indeed, the range of possible $T_{\text{CMB}}^{\text{is}}$ values
521 widen from a 50 K range (3920 to 3970 K) to a 230 K range (3891 to 4120 K) when
522 k increases from 0.6 to 0.925 and $\Delta = 100$ (Figure 8, panel c.). This widening of
523 the range of solutions is mostly borne by the higher temperature (and concomitantly
524 higher Si and higher O) solutions rather than lower temperature solutions. This
525 relates to the selection in input parameters presented in Figure 6: increasing the
526 value of k allows for solution to happen for lower values of λ , thus increasing the
527 average \overline{P}_{eq} during accretion and consequently the values of $T_{\text{CMB}}^{\text{is}}$, $w_{\text{Si}}^{\text{core}}$ and $w_{\text{O}}^{\text{core}}$
528 are increased. Increasing the metallic equilibrium therefore allows for models with a
529 steady increase of the magma ocean depth throughout accretion (lower values of λ)
530 to yield chemically coherent models, those models yielding then higher temperatures
531 for their cores. Decreasing the metallic equilibrium tends to select lower temperature
532 solutions. The difficulty of isolating an effect of k on the core composition is due to
533 two competitive phenomenon:

- 534 • Decreasing k tends to necessitate an increase in a_p (maximum pressure of equilib-
535 rium, see Figure 6) to obtain the right mantle composition, which in turn tends to
536 increase the concentration of Si and O in the core.
- 537 • Decreasing k means, by definition, to increase the amount of metal that does
538 not react with the mantle and keeps the same initial composition. Because the

Table 2: Results of the fit for Equation 23 for different values of k . The logarithmic dependency of the different temperature on the Δ and k values is quite clear for the minimum and mean temperature, and less obvious for the maximum temperature.

T_x	a_x	b_x	c_x
$T_{CMB}^{is} \text{ min}$	-63.92 ± 1.79	-58.77 ± 6.93	4065 ± 6.98
$\overline{T_{CMB}^{is}}$	-39.63 ± 0.74	78.46 ± 2.89	3970 ± 2.90
$T_{CMB}^{is} \text{ max}$	25.46 ± 4	375 ± 15.86	$3739 \pm$

539 initial concentrations of Si and O in the metal are very low, this tends to lower the
 540 concentration of Si and O in the core

541 From our data, it is not possible to distinguish which of the two phenomena takes
 542 over. As the range of possibility increases with the values of Δ , which phenomena
 543 takes over might be very specific to the value of Δ , a_p and λ . Untangling this
 544 question would necessitate further study beyond the scope of this one.

545 4.4 Quantitative relationship between temperature and chemical equilibrium

546 Figure 9 shows that the values of CMB temperature decrease with the logarithm of
 547 Δ , an effect that is counterbalanced linearly when increasing the value of k . This
 548 effect is easier to see for $\overline{T_{CMB}^{is}}$ (middle panel Figure 9), with the highest value of
 549 $\overline{T_{CMB}^{is}}$ on the top left corner of the solution space (high k , low Δ) and the lowest
 550 values on the bottom right corner of the solution (low k , high Δ). Therefore it is
 551 possible to quantify the evolution of the primitive core temperature as a function
 552 of Δ and k . In Figure 9, we can summarize the effect of k and Δ to the following
 553 equation:

$$T_x = a_x \log \Delta + b_x \log k + c_x \quad (23)$$

554 where, T_x stands for the minimum, mean or maximum value of T_{CMB}^{is} and a_x , b_x and
 555 c_x are the fitted parameter (in K) for each temperature. The results of the fit are
 556 presented in Table 2. The core temperature dependency with the silicate dilution
 557 Δ is higher when most of the metal is equilibrated. This is partly due to the lack
 558 of solutions, which tends to skew the value of temperature towards higher Δ values,
 559 but is also an effect of the disequilibrium in the metal: as the k is lowered, the
 560 temperature decreases but the number of solutions decreases with it. The values

561 given in Table 2 can yield a first approximation on the thermal state of the core for
562 a given model is affected by disequilibrium. Indeed, most partitioning models assume
563 equilibrium of the silicate on large scale (among other examples [Rubie et al., 2011](#);
564 [Jacobson et al., 2017](#); [Grewal et al., 2019](#); [Suer et al., 2021](#); [Loroch et al., 2024](#)), due
565 to fast convecting mantle silicate ([Höink et al., 2006](#); [Deguen et al., 2014](#)) reacting
566 with falling metallic spheres. These types of models will imply a lower temperature
567 of the primitive core, thus favoring the cold core hypothesis of [Nomura et al. \(2014\)](#),
568 [Davies et al. \(2015\)](#) or [Dobrosavljevic et al. \(2022\)](#) (CMB temperature of $\sim 3500 -$
569 4000 K). Studies focusing on the Hf/W partitioning and the moon forming impact
570 ([Rudge et al., 2010](#); [Nimmo et al., 2010](#); [Fischer and Nimmo, 2018](#)) tend to yield
571 lower values of metal equilibrium, with values of $k \sim 0.3 - 0.6$, to account for the
572 large size of the last impact. The value of $k = 0.3$ is also taken as a reference value
573 for the sensitivity study of [Gu et al. \(2023\)](#). According to our results, these models
574 will tend to favor also a cold core at the end of accretion: with $k = 0.6$ (higher end
575 of the range proposed by [Nimmo et al., 2010](#)), the maximum temperature will be \sim
576 4050 K for low silicate equilibrium ($\Delta \sim 4$) and ~ 3950 K for full mantle equilibrium
577 according to equation 23.

578 On the other hand, some models favor the hot core hypothesis, for instance
579 [Andrault et al. \(2017\)](#) or [Driscoll and Davies \(2023\)](#) (CMB temperatures above 5000
580 K); and some models tends to favor higher core temperatures right after accretion,
581 for instance [King and Olson \(2011\)](#) who proposed a mechanism allowing a higher
582 intake of gravitational dissipation energy by the metallic phase, thus leading to a hot
583 core right after accretion.

584 While the cold core hypothesis is easy to explain with classical accretion scenarios
585 such as proposed in this paper, the hot core hypothesis necessitates more hypothesis:
586 if we take the parameters in Table 2, and assume the temperature at the CMB
587 after accretion is the same as the temperature estimated by [Andrault et al. \(2017,](#)
588 $T_{CMB} = 5000K$), for $k = 1$, no value of Δ can yield this temperature. The
589 closest one are for Δ ranging from **6** and **50** to reach 4000 K at the CMB. Getting

590 high temperatures by disequilibrium alone is therefore not possible, and necessitates
591 other mechanisms which can add more heat to the core: for instance gravitational
592 dissipation energy intake (King and Olson, 2011; Clesi and Deguen, 2023), radiogenic
593 element partitioning (Faure et al., 2020), or a combination of several mechanisms
594 (Driscoll and Davies, 2023). However, what our results show, is that in order to
595 obtain a hot core at the end of accretion, the amount of additional heat added to
596 the core by these processes is lower if there is some chemical disequilibrium, yielding
597 higher concentrations of light elements into the core.

598 As a final note, these results are dependent on the hypothesis that there is a
599 thermal equilibrium of the metal at the bottom of the magma ocean, but not a
600 chemical equilibrium. This hypothesis is not unreasonable: the thermal diffusivity
601 within metallic alloys falls into the range of $\sim 10^{-6} \text{ m}^2.\text{s}^{-1}$ (Monaghan and Queded,
602 2001; Wilthan et al., 2015); and the chemical diffusivity of the elements within a
603 metallic alloy ranges between $\sim 10^{-9} \text{ m}^2.\text{s}^{-1}$ for Si or O (Posner et al., 2017a,b)
604 to $10^{-8} \text{ m}^2.\text{s}^{-1}$ for self diffusion of Fe (Dobson, 2002). Therefore, if the chemical
605 equilibrium is controlled by the diffusivity of element, it should be 100 to 1000 times
606 slower than the thermal equilibrium. A way to improve the results would be to also
607 couple thermal and chemical equilibrium by taking into account the advective controls
608 in equilibrium: both the heat and the chemical component can be transported by
609 the movements of metal and silicate in a turbulent flow (e.g. Deguen et al., 2014;
610 Wacheul and Le Bars, 2018; Clesi et al., 2020).

611 5 Conclusions

612 To conclude, we used a previously developed method to quantify the effect of
613 chemical disequilibrium on the thermal state of the core at the end of accretion.
614 Our model shows that at least 60% of the accreting metallic phase needs to be in
615 equilibrium with the silicate phase. Depending on the amount of metal equilibrated,
616 the dilution factor of the metal in the silicate needs to be >4 if $k = 1$ and >40 if

617 $k = 0.6$. This minimum value of $k = 0.6$ implies a rapid formation of the Earth's
618 core, up to ~ 50 millions years, according to the Hf-W chronometer.

619 As the degree of equilibrium, in particular in the silicate, is decreased, the average
620 pressure of equilibrium in the magma ocean needs to be increased to obtain a chem-
621 ically coherent BSE. This increase in the average pressure of equilibrium translates
622 directly into a higher initial core temperature. However, the maximum temperatures
623 obtained from the minimum equilibrium ($T_{CMB}^{is} \sim 4200K$) is not enough to account
624 for the hot core hypothesis, with 800 to 1000 K unaccounted for. Other mechanisms
625 increasing the core temperature are needed to produce a hot core, in particular
626 gravitational heat dissipation.

627 Further studies are needed in order to fully comprehend the accretion process and
628 the thermal evolution of the early core. In particular, the thermal model must be
629 enhanced to account for more element and better equation of state for the metal.

630 Enhancing the model, and in particular the implications for the Hf-W age of core
631 formation, will necessitate to link the degree of disequilibrium to the dynamic of
632 metal-silicate segregation throughout the entire process of accretion.

633 Acknowledgments

634 This work was supported by the European Research Council (ERC) under the Eu-
635 ropean Unions Horizon 2020 research and innovation programme (grant number
636 716429). ISTerre is part of Labex OSUG@2020 (ANR10 LABX56).

637 Data, code, and outputs availability

638 The initial code used to generate the model from Clesi and Deguen (2023) can be
639 accessed freely at the following link: <https://doi.org/10.5281/zenodo.7661374>. A
640 tutorial on the chemical part is accessible in the supplementary material of Clesi
641 and Deguen (2024a) (open access) at the following link <https://doi.org/10.1016/j>.

642 [chemgeo.2024.122104](https://doi.org/10.5281/zenodo.18940615). The code used to generate the rest of the figures is available
643 at the following link: <https://doi.org/10.5281/zenodo.18940615>.

644 **Competing interests**

645 The authors declare no competing interests.

646 **Licence agreement**

647 This article is distributed under the terms of the Creative Commons Attribution
648 4.0 International Licence (CC BY 4.0), which permits unrestricted use, distribution,
649 and reproduction in any medium, provided appropriate credit is given to the original
650 author(s) and source, as well as a link to the Creative Commons licence, and an
651 indication of changes that were made.

652 **References**

- 653 Al'Tshuler, L., Brusnikin, S. and Kuz'Menkov, E. (1987). Isotherms and Grüneisen functions for 25
654 metals. *Journal of Applied Mechanics and Technical Physics* 28: 129–141.
- 655 Andrault, D., Bolfan-Casanova, N., Bouhifd, M., Boujibar, A., Garbarino, G., Manthilake, G.,
656 Mezouar, M., Monteux, J., Parisiades, P. and Pesce, G. (2017). Toward a coherent model for
657 the melting behavior of the deep earth's mantle. *Physics of the Earth and Planetary Interiors* 265:
658 67–81.
- 659 Andrault, D., Bolfan-Casanova, N., Nigro, G. L., Bouhifd, M. A., Garbarino, G. and Mezouar, M.
660 (2011). Solidus and liquidus profiles of chondritic mantle: Implication for melting of the Earth
661 across its history. *Earth and planetary science letters* 304: 251–259.
- 662 Birch, F. (1965). Energetics of core formation. *Journal of Geophysical research* 70: 6217–6221.
- 663 Bouhifd, M. and Jephcoat, A. (2011). Convergence of Ni and Co metal–silicate partition coefficients
664 in the deep magma-ocean and coupled silicon–oxygen solubility in iron melts at high pressures.
665 *Earth and Planetary Science Letters* 307: 341–348.

- 666 Bouhifd, M. A., Gautron, L., Bolfan-Casanova, N., Malavergne, V., Hammouda, T., Andrault, D. and
667 Jephcoat, A. (2007). Potassium partitioning into molten iron alloys at high-pressure: Implications
668 for Earth's core. *Physics of the Earth and Planetary Interiors* 160: 22–33.
- 669 Clesi, V., Bouhifd, M., Bolfan-Casanova, N., Manthilake, G., Fabbriozio, A. and Andrault, D. (2016).
670 Effect of H₂O on metal–silicate partitioning of Ni, Co, V, Cr, Mn and Fe: Implications for the
671 oxidation state of the Earth and Mars. *Geochimica et Cosmochimica Acta* 192: 97–121.
- 672 Clesi, V. and Deguen, R. (2023). Linking the core heat content to earth's
673 accretion history. *Geochemistry, Geophysics, Geosystems* 24: e2022GC010661,
674 doi:<https://doi.org/10.1029/2022GC010661>.
- 675 Clesi, V. and Deguen, R. (2024a). Effect of discretization choices when modeling the thermo-chemical
676 history of the accreting core. *Chemical Geology* 657: 122104.
- 677 Clesi, V. and Deguen, R. (2024b). Grüneisen parameter formalism in the study of the earth's core
678 formation: a sensitivity study. *Geophysical Journal International* 237: 1275–1284.
- 679 Clesi, V., Monteux, J., Qaddah, B., Le Bars, M., Wacheul, J.-B. and Bouhifd, M. A. (2020). Dynamics
680 of core-mantle separation: Influence of viscosity contrast and metal/silicate partition coefficients
681 on the chemical equilibrium. *Physics of the Earth and Planetary Interiors* 306: 106547.
- 682 Davies, C., Pozzo, M., Gubbins, D. and Alfe, D. (2015). Constraints from material properties on the
683 dynamics and evolution of earth's core. *Nature Geoscience* 8: 678–685.
- 684 Deguen, R., Landeau, M. and Olson, P. (2014). Turbulent metal–silicate mixing, fragmentation, and
685 equilibration in magma oceans. *Earth and Planetary Science Letters* 391: 274–287.
- 686 Dobrosavljevic, V. V., Zhang, D., Sturhahn, W., Zhao, J., Toellner, T. S., Chariton, S., Prakapenka,
687 V. B., Pardo, O. S. and Jackson, J. M. (2022). Melting and phase relations of fe-ni-si determined
688 by a multi-technique approach. *Earth and Planetary Science Letters* 584: 117358.
- 689 Dobson, D. P. (2002). Self-diffusion in liquid fe at high pressure. *Physics of the Earth and Planetary*
690 *Interiors* 130: 271–284.
- 691 Drake, M. J. and Richter, K. (2002). Determining the composition of the Earth. *Nature* 416: 39–44.
- 692 Driscoll, P. and Davies, C. (2023). The “new core paradox:” challenges and potential solutions. *Journal*
693 *of Geophysical Research: Solid Earth* : e2022JB025355.
- 694 Dziewonski, A. M. and Anderson, D. L. (1981). Preliminary reference Earth model. *Physics of the*
695 *earth and planetary interiors* 25: 297–356.

- 696 Faure, P., Bouhifd, M. A., Boyet, M., Manthilake, G., Clesi, V. and Devidal, J.-L. (2020). Uranium and
697 thorium partitioning in the bulk silicate Earth and the oxygen content of Earth's core. *Geochimica*
698 *et Cosmochimica Acta* 275: 83–98.
- 699 Fischer, R. A., Campbell, A. J. and Ciesla, F. J. (2017). Sensitivities of earth's core and mantle
700 compositions to accretion and differentiation processes. *Earth and Planetary Science Letters* 458:
701 252–262.
- 702 Fischer, R. A., Nakajima, Y., Campbell, A. J., Frost, D. J., Harries, D., Langenhorst, F., Miyajima,
703 N., Pollok, K. and Rubie, D. C. (2015). High pressure metal–silicate partitioning of Ni, Co, V, Cr,
704 Si, and O. *Geochimica et Cosmochimica Acta* 167: 177–194.
- 705 Fischer, R. A. and Nimmo, F. (2018). Effects of core formation on the hf–w isotopic composition
706 of the earth and dating of the moon-forming impact. *Earth and planetary science letters* 499:
707 257–265.
- 708 Frost, D. J., Asahara, Y., Rubie, D. C., Miyajima, N., Dubrovinsky, L. S., Holzapfel, C., Ohtani, E.,
709 Miyahara, M. and Sakai, T. (2010). Partitioning of oxygen between the Earth's mantle and core.
710 *Journal of Geophysical Research: Solid Earth* 115.
- 711 Grewal, D. S., Dasgupta, R., Sun, C., Tsuno, K. and Costin, G. (2019). Delivery of carbon, nitrogen,
712 and sulfur to the silicate Earth by a giant impact. *Science advances* 5: eaau3669.
- 713 Gu, J. T., Fischer, R. A., Brennan, M. C., Clement, M. S., Jacobson, S. A., Kaib, N. A., O'Brien,
714 D. P. and Raymond, S. N. (2023). Comparisons of the core and mantle compositions of earth
715 analogs from different terrestrial planet formation scenarios. *Icarus* 394: 115425.
- 716 Höink, T., Schmalzl, J. and Hansen, U. (2006). Dynamics of metal-silicate separation in a terrestrial
717 magma ocean. *Geochemistry, Geophysics, Geosystems* 7.
- 718 Izidoro, A., Bitsch, B. and Dasgupta, R. (2021). The effect of a strong pressure bump in the Sun's
719 natal disk: terrestrial planet formation via planetesimal accretion rather than pebble accretion. *The*
720 *Astrophysical Journal* 915: 62.
- 721 Jacobson, S. A., Rubie, D. C., Hernlund, J., Morbidelli, A. and Nakajima, M. (2017). Formation,
722 stratification, and mixing of the cores of Earth and Venus. *Earth and Planetary Science Letters*
723 474: 375–386.
- 724 King, C. and Olson, P. (2011). Heat partitioning in metal-silicate plumes during Earth differentiation.
725 *Earth and Planetary Science Letters* 304: 577–586.

- 726 Landeau, M., Deguen, R., Phillips, D., Neufeld, J. A., Lherm, V. and Dalziel, S. B. (2021). Metal-
727 silicate mixing by large Earth-forming impacts. *Earth and Planetary Science Letters* 564: 116888.
- 728 Loroch, D., Hackler, S., Rohrbach, A., Berndt, J. and Klemme, S. (2024). Accretion and core
729 formation of earth-like planets: Insights from metal–silicate partitioning of siderophile and volatile
730 elements. *Geosciences* 14: 281.
- 731 McDonough, W. and Sun, S.-S. (1995). The composition of the Earth. *Chemical geology* 120: 223–
732 253.
- 733 Monaghan, B. and Queded, P. (2001). Thermal diffusivity of iron at high temperature in both the
734 liquid and solid states. *ISIJ international* 41: 1524–1528.
- 735 Monteux, J., Ricard, Y., Coltice, N., Dubuffet, F. and Ulvrova, M. (2009). A model of metal–silicate
736 separation on growing planets. *Earth and Planetary Science Letters* 287: 353–362.
- 737 Morbidelli, A., Chambers, J., Lunine, J., Petit, J.-M., Robert, F., Valsecchi, G. and Cyr, K. (2000).
738 Source regions and timescales for the delivery of water to the Earth. *Meteoritics & Planetary
739 Science* 35: 1309–1320.
- 740 Nimmo, F., O'Brien, D. and Kleine, T. (2010). Tungsten isotopic evolution during late-stage accretion:
741 constraints on earth–moon equilibration. *Earth and Planetary Science Letters* 292: 363–370.
- 742 Nomura, R., Hirose, K., Uesugi, K., Ohishi, Y., Tsuchiyama, A., Miyake, A. and Ueno, Y. (2014). Low
743 core–mantle boundary temperature inferred from the solidus of pyrolite. *Science* 343: 522–525.
- 744 Posner, E. S., Rubie, D. C., Frost, D. J. and Steinle-Neumann, G. (2017a). Experimental
745 determination of oxygen diffusion in liquid iron at high pressure. *Earth and Planetary Science
746 Letters* 464: 116–123.
- 747 Posner, E. S., Rubie, D. C., Frost, D. J., Vlček, V. and Steinle-Neumann, G. (2017b). High p–t
748 experiments and first principles calculations of the diffusion of si and cr in liquid iron. *Geochimica
749 et Cosmochimica Acta* 203: 323–342.
- 750 Pu, C., Gao, X., Wu, Z., Du, Z. and Jing, Z. (2025). Metal-silicate partitioning of si, o, and mg at
751 high pressures and high temperatures: Implications to the compositional evolution of core-forming
752 metallic melts. *Geochemistry, Geophysics, Geosystems* 26: e2024GC011940.
- 753 Raymond, S. N., O'Brien, D. P., Morbidelli, A. and Kaib, N. A. (2009). Building the terrestrial planets:
754 Constrained accretion in the inner Solar System. *Icarus* 203: 644–662.

- 755 Rubie, D., Frost, D., Mann, U., Asahara, Y., Nimmo, F., Tsuno, K., Kegler, P., Holzheid, A. and
756 Palme, H. (2011). Heterogeneous accretion, composition and core–mantle differentiation of the
757 Earth. *Earth and Planetary Science Letters* 301: 31–42.
- 758 Rubie, D., Jacobson, S., Morbidelli, A., O'Brien, D., Young, E., Vries, J. de, Nimmo, F., Palme, H.
759 and Frost, D. (2015). Accretion and differentiation of the terrestrial planets with implications for
760 the compositions of early-formed Solar System bodies and accretion of water. *Icarus* 248: 89–108.
- 761 Rubie, D., Melosh, H., Reid, J., Liebske, C. and Righter, K. (2003). Mechanisms of metal–silicate
762 equilibration in the terrestrial magma ocean. *Earth and Planetary Science Letters* 205: 239–255.
- 763 Rudge, J. F., Kleine, T. and Bourdon, B. (2010). Broad bounds on earth's accretion and core
764 formation constrained by geochemical models. *Nature Geoscience* 3: 439–443.
- 765 Samuel, H. (2012). A re-evaluation of metal diapir breakup and equilibration in terrestrial magma
766 oceans. *Earth and Planetary Science Letters* 313: 105–114.
- 767 Samuel, H., Tackley, P. and Evonuk, M. (2010). Heat partitioning in terrestrial planets during core
768 formation by negative diapirism. *Earth and Planetary Science Letters* 290: 13–19.
- 769 Siebert, J., Badro, J., Antonangeli, D. and Ryerson, F. J. (2012). Metal–silicate partitioning of Ni
770 and Co in a deep magma ocean. *Earth and Planetary Science Letters* 321: 189–197.
- 771 Suer, T.-A., Siebert, J., Remusat, L., Day, J. M., Borensztajn, S., Doisneau, B. and Fiquet, G. (2021).
772 Reconciling metal–silicate partitioning and late accretion in the earth. *Nature Communications* 12:
773 2913.
- 774 Ulvrová, M., Coltice, N., Ricard, Y., Labrosse, S., Dubuffet, F., Velínský, J. and Šrámek, O.
775 (2011). Compositional and thermal equilibration of particles, drops and diapirs in geophysical flows.
776 *Geochemistry Geophysics Geosystems* 12: 1–11.
- 777 Wacheul, J.-B. and Le Bars, M. (2018). Experiments on fragmentation and thermo-chemical
778 exchanges during planetary core formation. *Physics of the Earth and Planetary Interiors* 276: 134–
779 144.
- 780 Wade, J. and Wood, B. J. (2005). Core formation and the oxidation state of the earth. *Earth and*
781 *Planetary Science Letters* 236: 78–95.
- 782 Wasson, J. T. and Kallemeyn, G. W. (1988). Compositions of chondrites. *Philosophical Transactions*
783 *of the Royal Society of London. Series A, Mathematical and Physical Sciences* 325: 535–544.

- 784 Wilthan, B., Schützenhöfer, W. and Pottlacher, G. (2015). Thermal diffusivity and thermal
785 conductivity of five different steel alloys in the solid and liquid phases. *International Journal of*
786 *Thermophysics* 36: 2259–2272.
- 787 Wood, B., Wade, J. and Kilburn, M. (2008). Core formation and the oxidation state of the Earth:
788 Additional constraints from Nb, V and Cr partitioning. *Geochimica et Cosmochimica Acta* 72:
789 1415–1426.
- 790 Zhang, D., Jackson, J. M., Zhao, J., Sturhahn, W., Alp, E. E., Hu, M. Y., Toellner, T. S., Murphy,
791 C. A. and Prakapenka, V. B. (2016). Temperature of Earth's core constrained from melting of Fe
792 and Fe_{0.9}Ni_{0.1} at high pressures. *Earth and Planetary Science Letters* 447: 72–83.

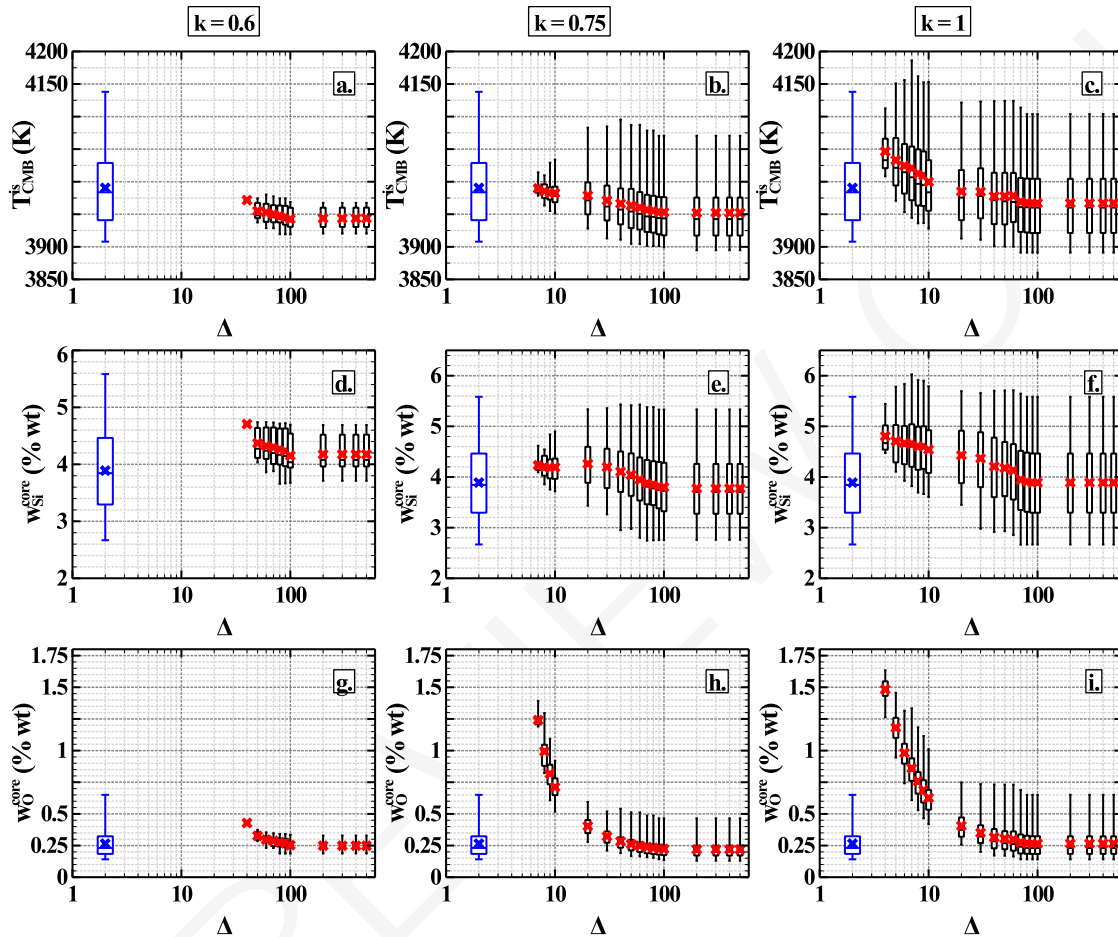


Figure 7: Effect of the silicate dilution Δ on the core properties (isentropic temperature at the CMB, light element content) for different values of k . First row, panels a. to c.: T_{CMB}^{is} in K. Second row, panels d. to f.: w_{Si}^{core} in % wt. Third row, panels g. to i.: w_O^{core} in % wt. The left, middle and right column shows the evolution of the parameters values for $k = 0.6$, $k = 0.75$ and $k = 1$, respectively. In each panel the entire solutions range are presented as boxplots, with the red cross being the mean value of the parameter, the white box delimiting the 1st and 3rd quartile, the horizontal line the median value and the vertical lines the minimum and maximum values. The reference model dataset is presented in blue with the same type of plot for comparison, in an arbitrary position for readability.

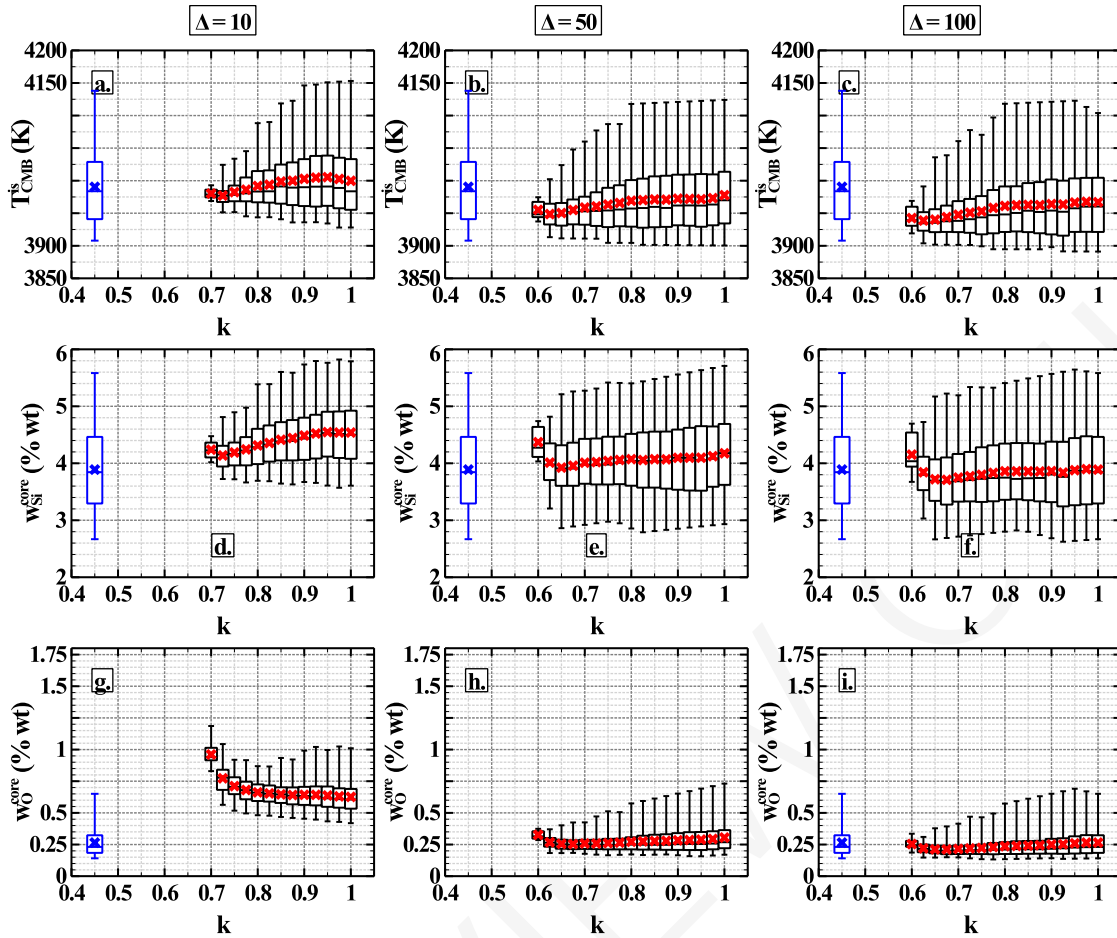


Figure 8: Effect of metal equilibrium k on the core properties (isentropic temperature at the CMB, light element content) for different values of Δ . First row, panels a. to c.: T_{CMB}^{is} in K. Second row, panels d. to f.: w_{Si}^{core} in % wt. Third row, panels g. to i.: w_O^{core} in % wt. The left, middle and right column shows the evolution of the parameters values for $\Delta = 10$, $\Delta = 50$ and $\Delta = 100$, respectively. In each panel the entire solutions range are presented as boxplots, with the red cross being the mean value of the parameter, the white box delimiting the 1st and 3rd quartile, the horizontal line the median value and the vertical lines the minimum and maximum values. The reference model dataset is presented in blue with the same type of plot for comparison, in an arbitrary position for readability.

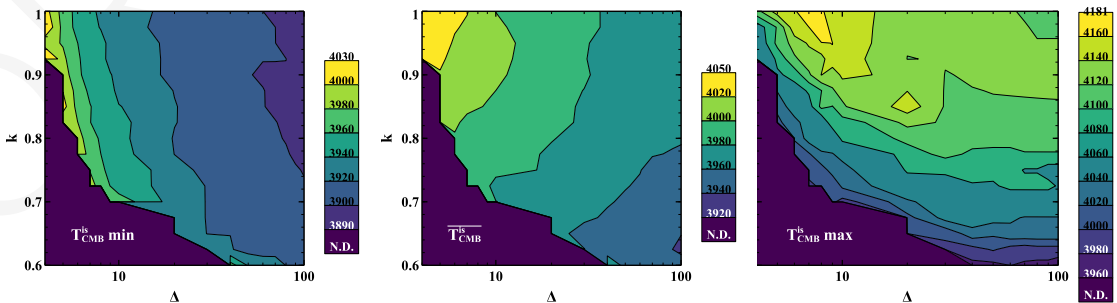


Figure 9: Evolution of minimum (left, $T_{CMB}^{is} min$), mean (center, $\overline{T_{CMB}^{is}}$) and maximum (right, $T_{CMB}^{is} max$) temperature at the CMB after isentropic mixing as a function of k (linear scale) and Δ (log scale). The color scale is changing from panel to panel to account for the different range of values (larger range for the maximum value, narrower range for mean and minimum values).

Supplementary information to "Effect of chemical disequilibrium during metal-silicate partitioning on the thermal state of the early core"

Vincent Clesi^{1,2} and Renaud Deguen^{2,3}

¹Institut für Mineralogie, Münster Universität, Correnstraße 24, 48149 Münster

²Univ Lyon, ENSL, UCBL, UJM, CNRS, LGL-TPE, F-69007 Lyon, France

³Univ. Grenoble Alpes, Univ. Savoie Mont Blanc, CNRS, IRD, Univ. Gustave Eiffel, ISTERre, 38000 Grenoble, France

ABSTRACT

This is the supplementary figures for the paper entitled 'Effect of chemical disequilibrium during metal-silicate partitioning on the thermal state of the early core'. Most of the figure are the final concentrations of each element in the mantle and the core (Fig. S4 to S19).

Keywords: Accretion model, Core temperature, metal silicate partitioning, magma ocean, core formation

REFERENCES

- Clesi, V. and Deguen, R. (2023). Linking the core heat content to earth's accretion history. *Geochemistry, Geophysics, Geosystems*, 24(5):e2022GC010661.
- Clesi, V. and Deguen, R. (2024). Effect of discretization choices when modeling the thermo-chemical history of the accreting core. *Chemical Geology*, 657:122104.

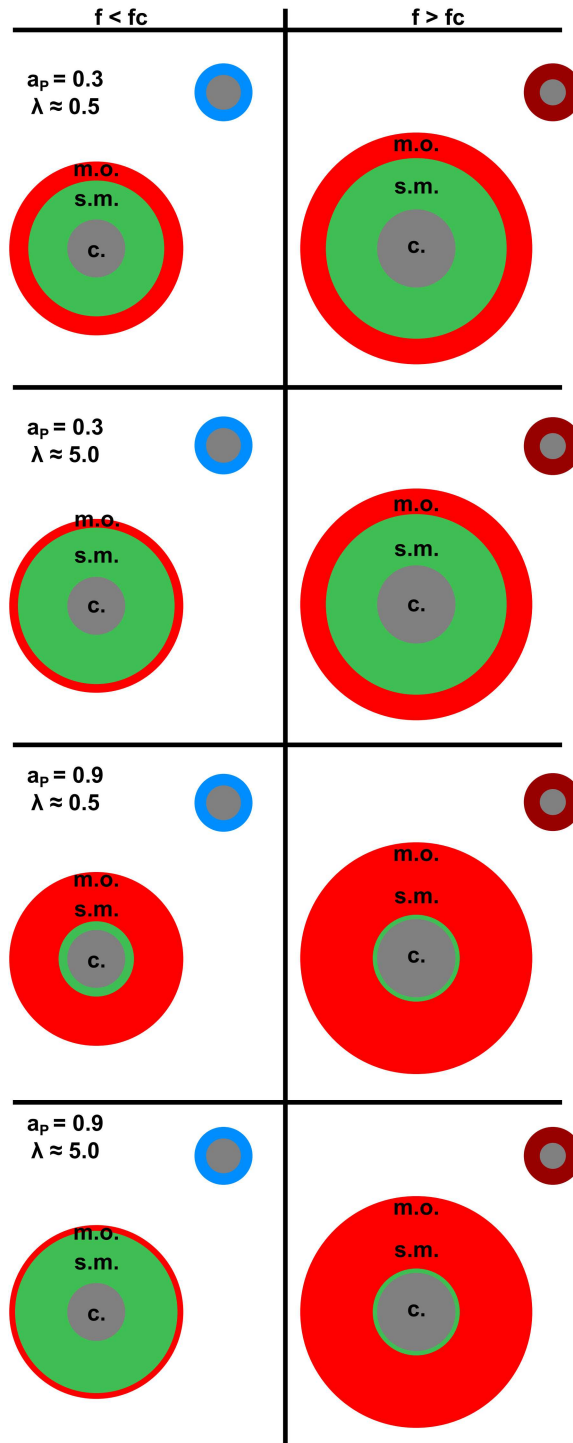


Figure S.1. Schematics of the physical meaning of the parameters a_p , f_c and λ used to parameterize the models of accretion. This Figure has been published in [Clesi and Deguen \(2024\)](#) and is reproduced here with the authorization of authors. The left column shows the early part of accretion ($f < f_c$, more reduced impactor in blue). The right column shows the later stage of accretion ($f > f_c$, more oxidized impactor in dark red). The two first lines show the effect of λ for a low value of a_p on the depth of the magma ocean throughout accretion. The two bottom lines show the effect of λ for a high value of a_p on the evolution of the depth of the magma ocean during accretion. m.o. = magma ocean (red), s.m. = solid mantle (green) and c. = core (grey).

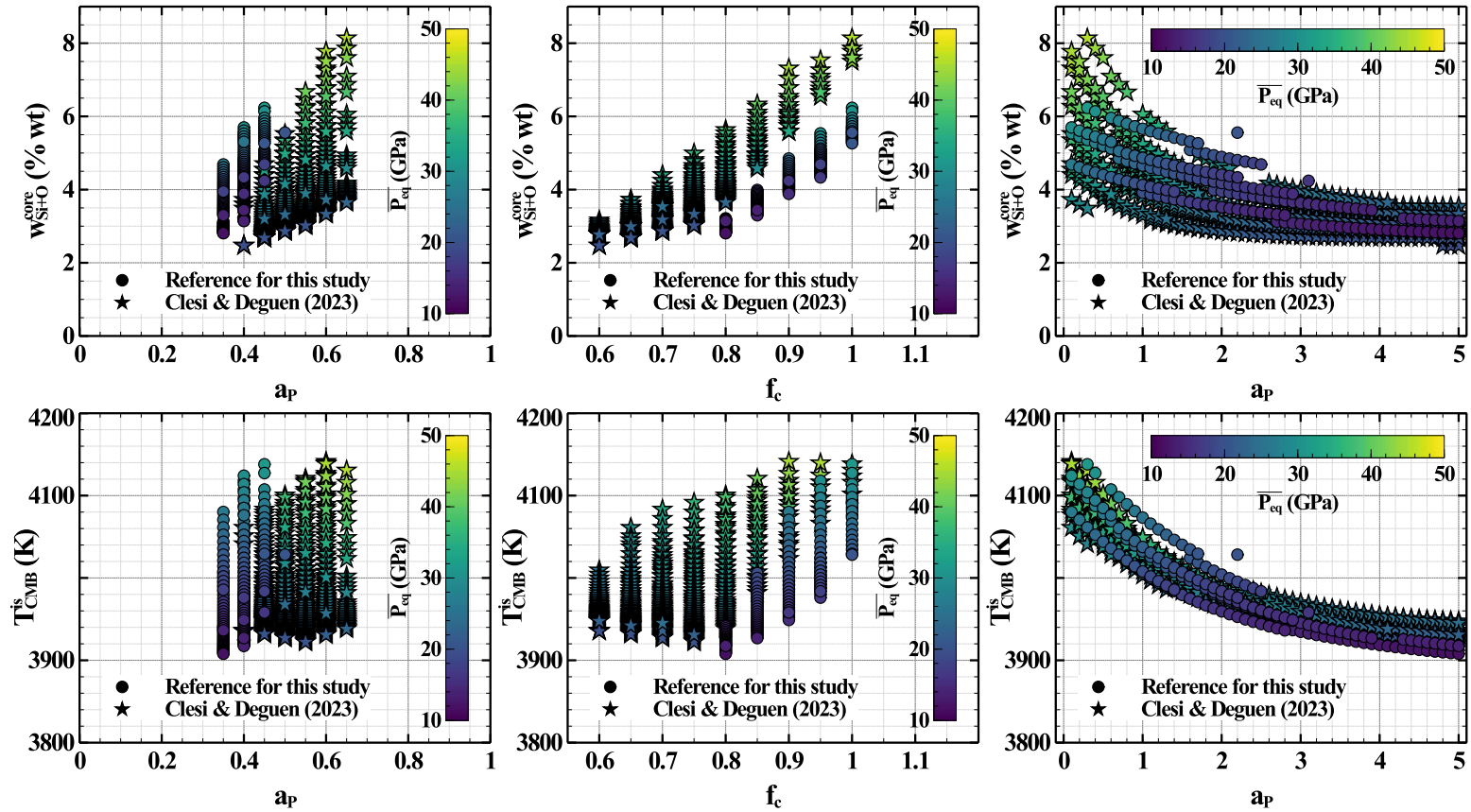


Figure S.2. Comparison of the reference solutions that are used in this study (round symbols) with the solutions obtained in [Clesi and Deguen \(2023\)](#) with another filter (stars). The format of this figure is the derived from Figure 8 of [Clesi and Deguen \(2023\)](#) to better highlight the differences between the solutions. The overall correlations are the same, with the weighted mean filter selecting for higher pressures models. The first row shows the correlation between light elements in the core with the three input parameters on each column: w_{Si+O}^{core} vs a_p on the left panel, w_{Si+O}^{core} vs f_c on the middle panel, w_{Si+O}^{core} vs λ on the right panel. The second row shows the correlation between the isentropic temperature at the CMB (T_{CMB}^{is}) with the three input parameters presented in the same order. The color scale in all panel is the composite input parameter \bar{P}_{eq} in GPa.

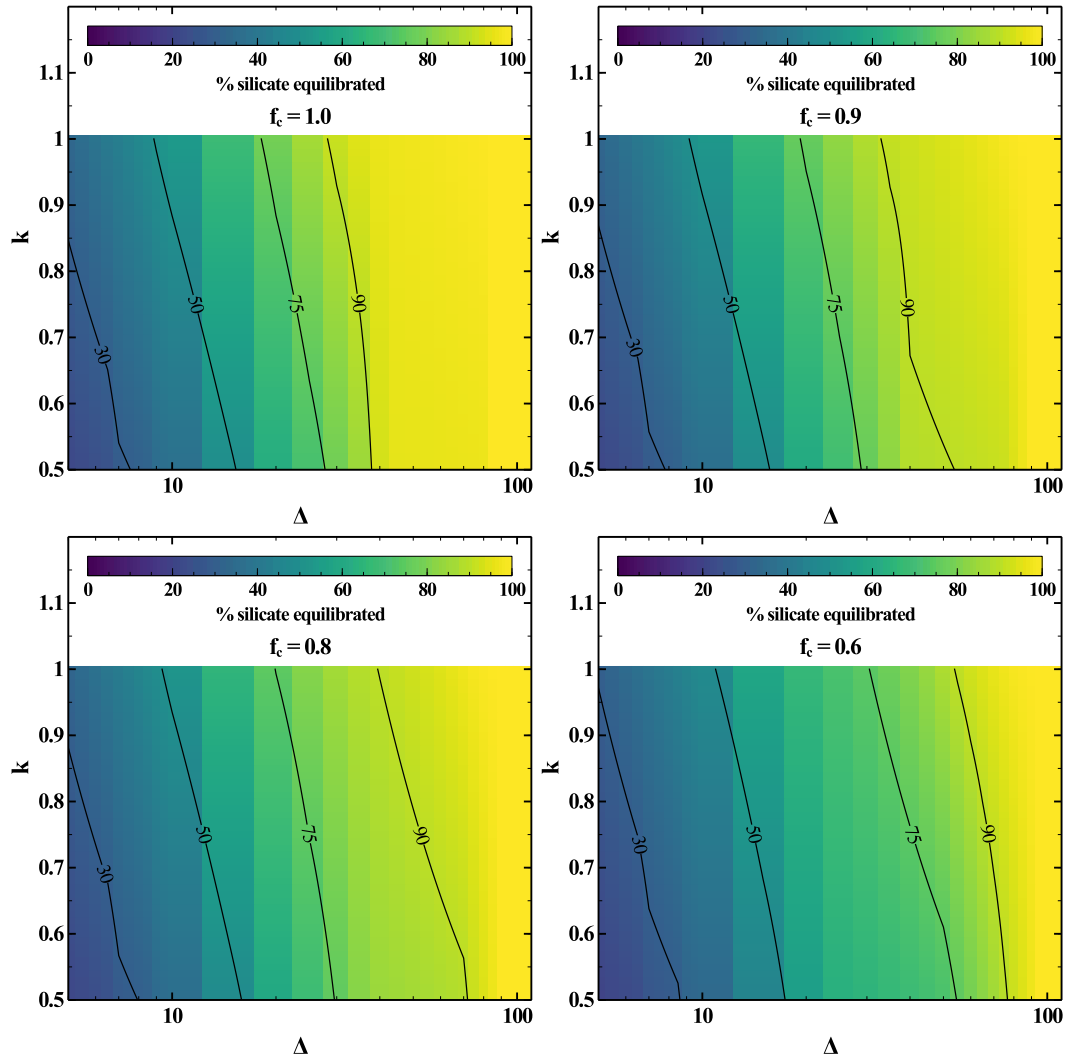


Figure S.3. Percentage of equilibrated mantle (color map) as a function of k (y-axis) and Δ (x-axis) for $f_c = 1$ (top left), $f_c = 0.9$ (top right), $f_c = 0.8$ (bottom left), $f_c = 0.6$ (bottom right). Full equilibrium is reached for $\Delta > 100$ in all relevant cases.

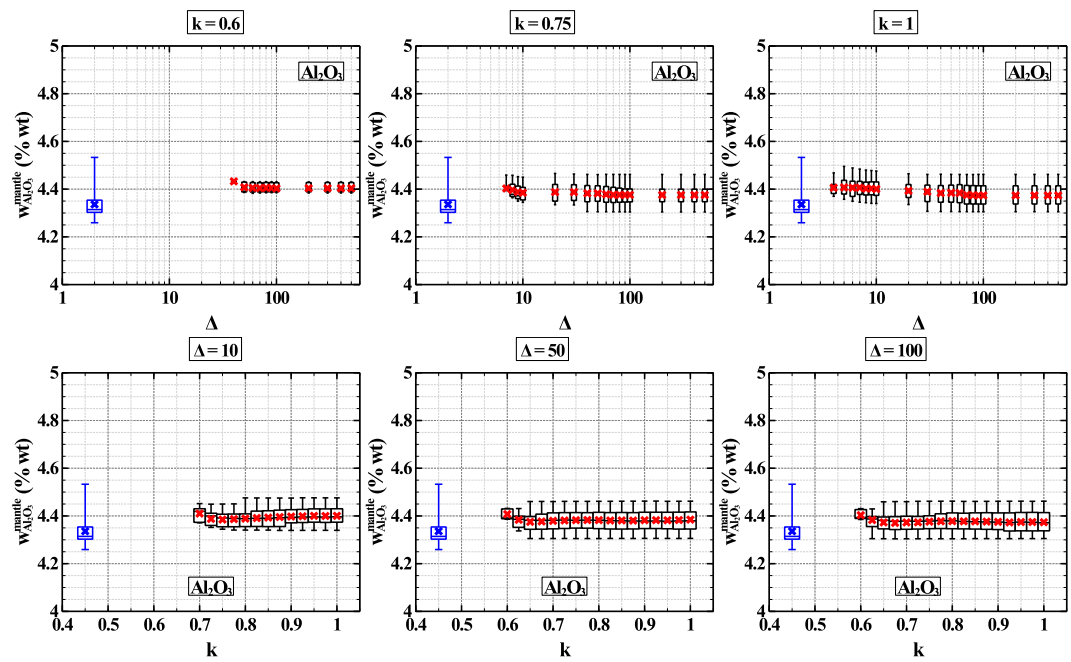


Figure S.4. Evolution of Al_2O_3 concentrations (% wt) in the mantle as a function of Δ for fixed values of k (top row), and as a function of k for fixed values of Δ (bottom row). In each panel the entire solutions range are presented as boxplots, with the red cross being the mean value of the parameter, the white box delimiting the 1st and 3rd quartile, the horizontal line the median value and the vertical lines the minimum and maximum values. The reference model dataset is presented in blue with the same type of plot for comparison.

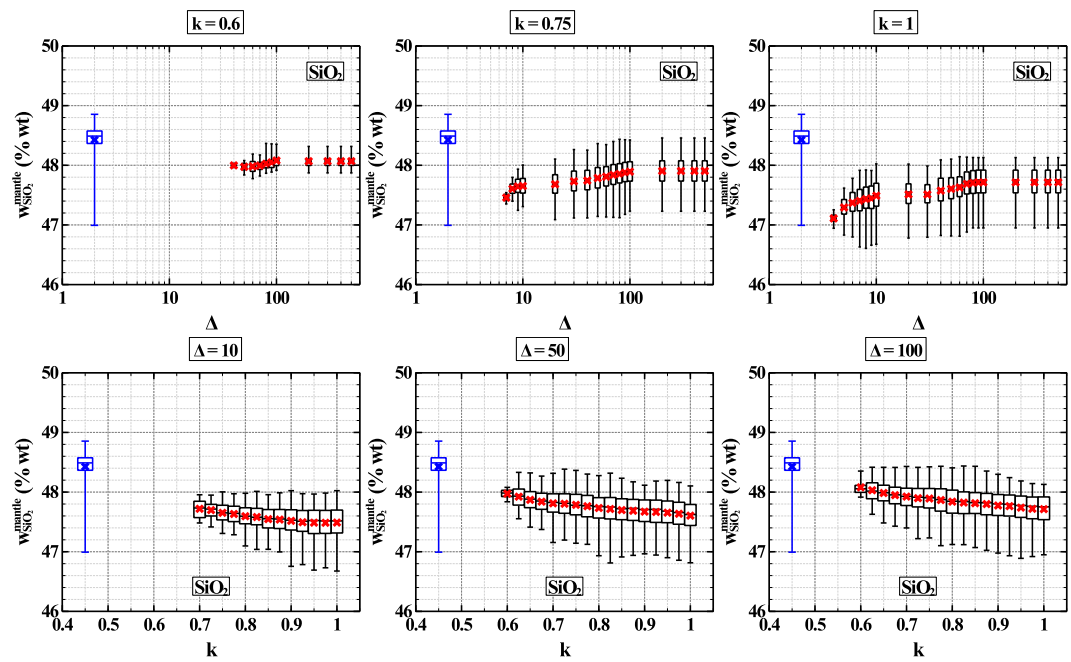


Figure S.5. Evolution of SiO_2 concentrations (% wt) in the mantle as a function of Δ for fixed values of k (top row), and as a function of k for fixed values of Δ (bottom row). In each panel the entire solutions range are presented as boxplots, with the red cross being the mean value of the parameter, the white box delimiting the 1st and 3rd quartile, the horizontal line the median value and the vertical lines the minimum and maximum values. The reference model dataset is presented in blue with the same type of plot for comparison.

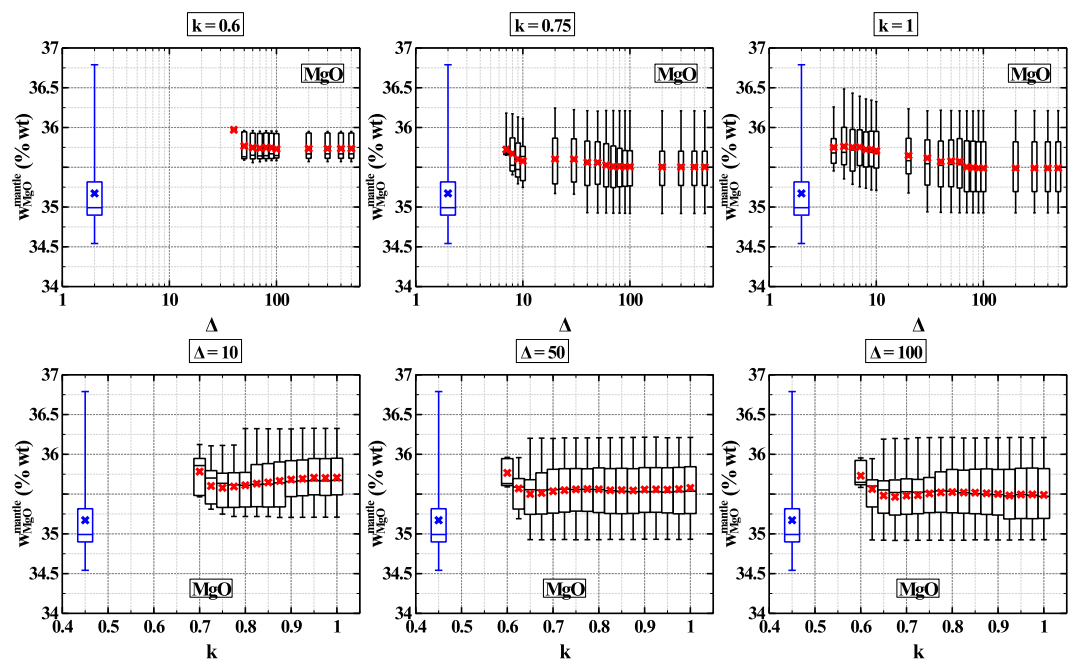


Figure S.6. Evolution of MgO concentrations (% wt) in the mantle as a function of Δ for fixed values of k (top row), and as a function of k for fixed values of Δ (bottom row). In each panel the entire solutions range are presented as boxplots, with the red cross being the mean value of the parameter, the white box delimiting the 1st and 3rd quartile, the horizontal line the median value and the vertical lines the minimum and maximum values. The reference model dataset is presented in blue with the same type of plot for comparison.

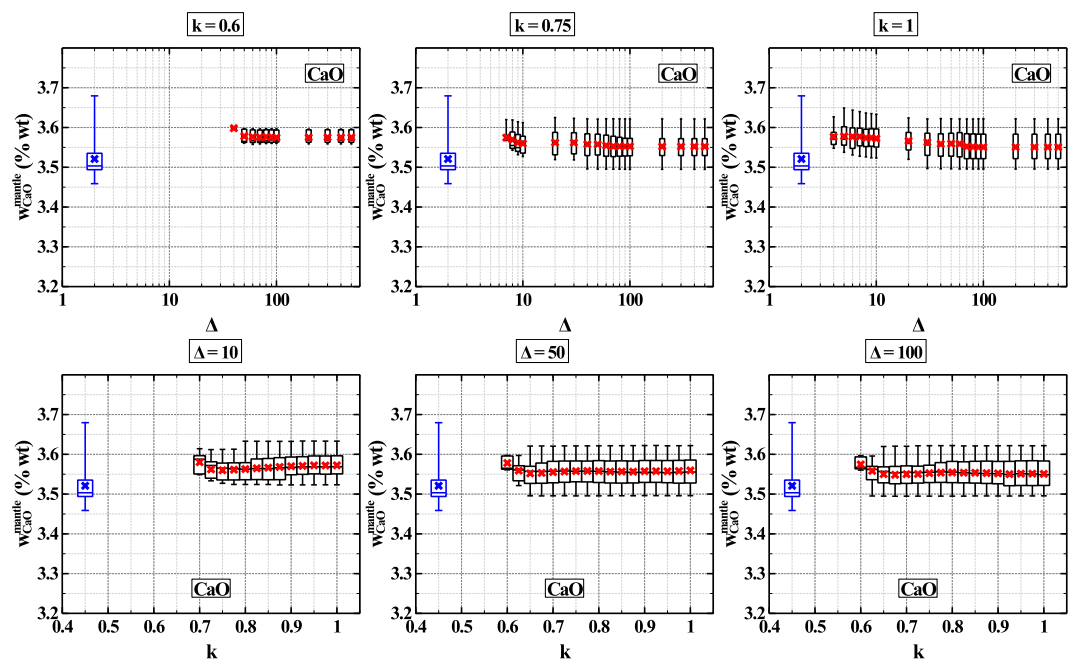


Figure S.7. Evolution of CaO concentrations (% wt) in the mantle as a function of Δ for fixed values of k (top row), and as a function of k for fixed values of Δ (bottom row). In each panel the entire solutions range are presented as boxplots, with the red cross being the mean value of the parameter, the white box delimiting the 1st and 3rd quartile, the horizontal line the median value and the vertical lines the minimum and maximum values. The reference model dataset is presented in blue with the same type of plot for comparison.

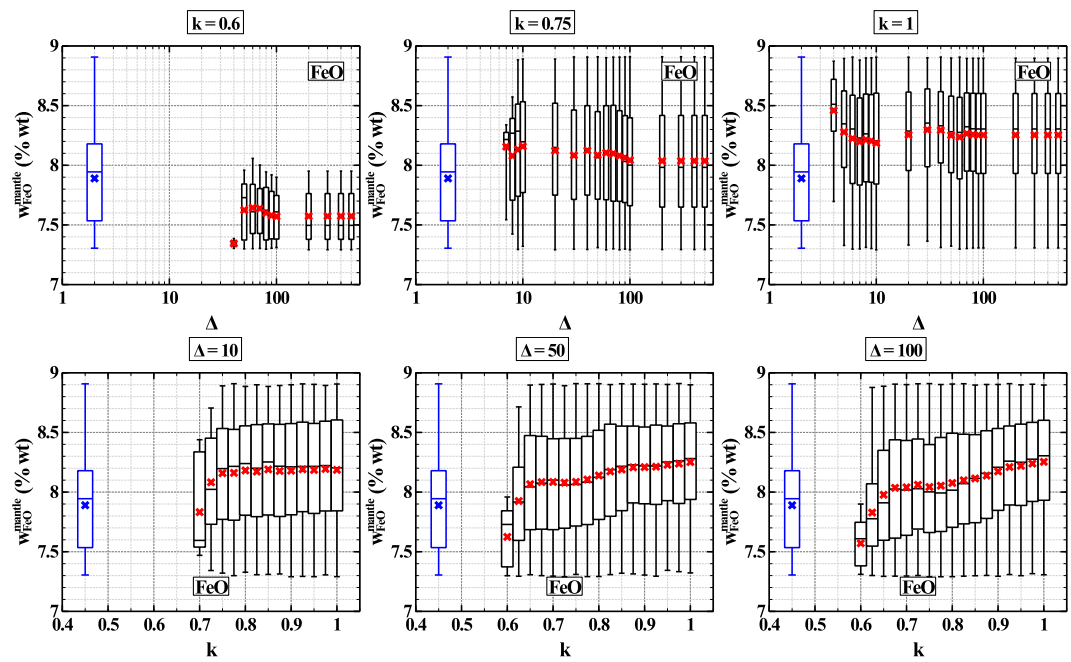


Figure S.8. Evolution of FeO concentrations (%wt) in the mantle as a function of Δ for fixed values of k (top row), and as a function of k for fixed values of Δ (bottom row). In each panel the entire solutions range are presented as boxplots, with the red cross being the mean value of the parameter, the white box delimiting the 1st and 3rd quartile, the horizontal line the median value and the vertical lines the minimum and maximum values. The reference model dataset is presented in blue with the same type of plot for comparison.

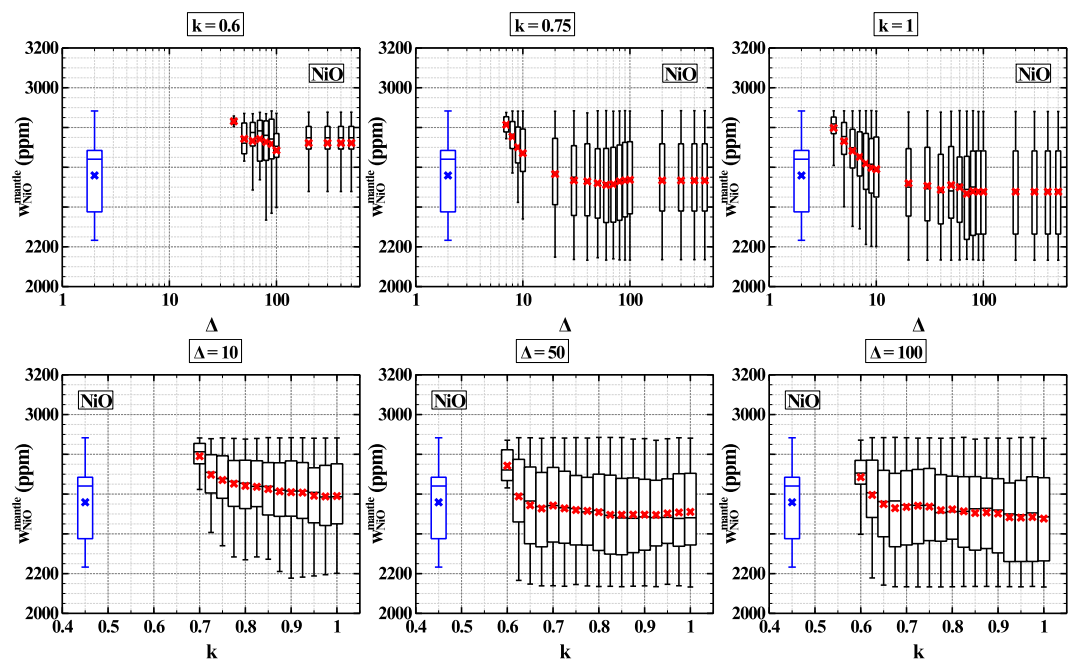


Figure S.9. Evolution of NiO concentrations (ppm) in the mantle as a function of Δ for fixed values of k (top row), and as a function of k for fixed values of Δ (bottom row). In each panel the entire solutions range are presented as boxplots, with the red cross being the mean value of the parameter, the white box delimiting the 1st and 3rd quartile, the horizontal line the median value and the vertical lines the minimum and maximum values. The reference model dataset is presented in blue with the same type of plot for comparison.

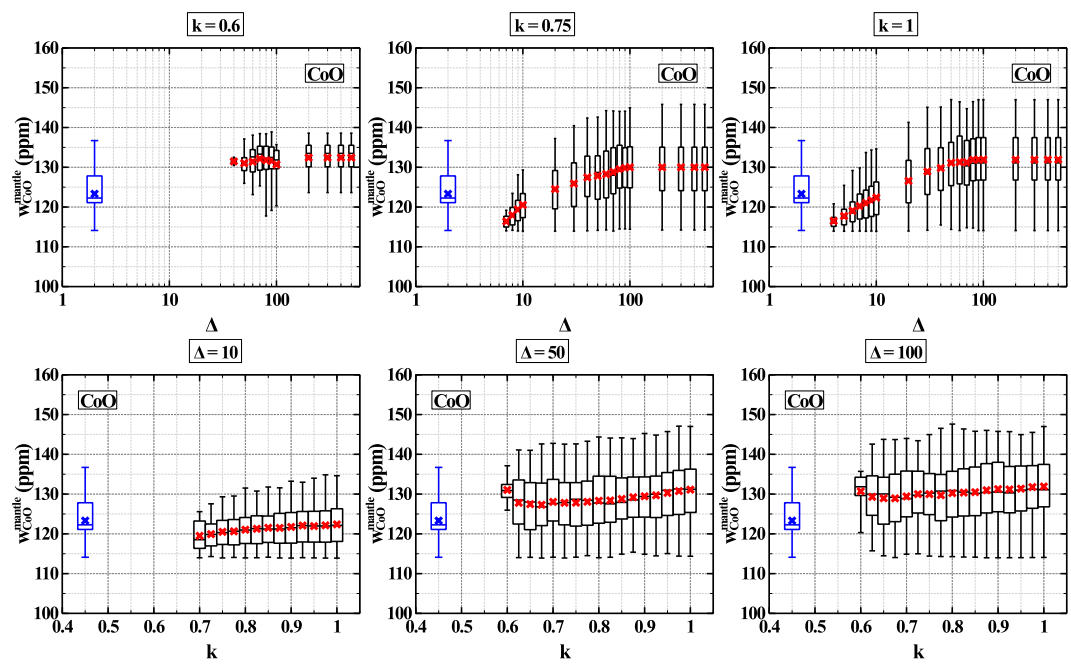


Figure S.10. Evolution of CoO concentrations (ppm) in the mantle as a function of Δ for fixed values of k (top row), and as a function of k for fixed values of Δ (bottom row). In each panel the entire solutions range are presented as boxplots, with the red cross being the mean value of the parameter, the white box delimiting the 1st and 3rd quartile, the horizontal line the median value and the vertical lines the minimum and maximum values. The reference model dataset is presented in blue with the same type of plot for comparison.

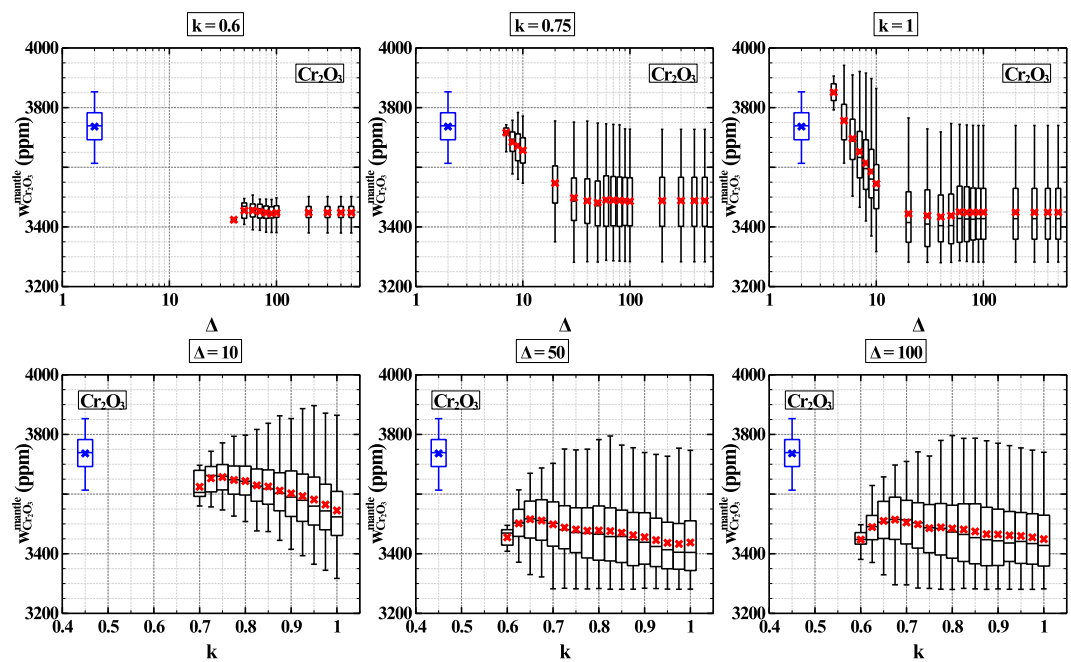


Figure S.11. Evolution of Cr_2O_3 concentrations (ppm) in the mantle as a function of Δ for fixed values of k (top row), and as a function of k for fixed values of Δ (bottom row). In each panel the entire solutions range are presented as boxplots, with the red cross being the mean value of the parameter, the white box delimiting the 1st and 3rd quartile, the horizontal line the median value and the vertical lines the minimum and maximum values. The reference model dataset is presented in blue with the same type of plot for comparison.

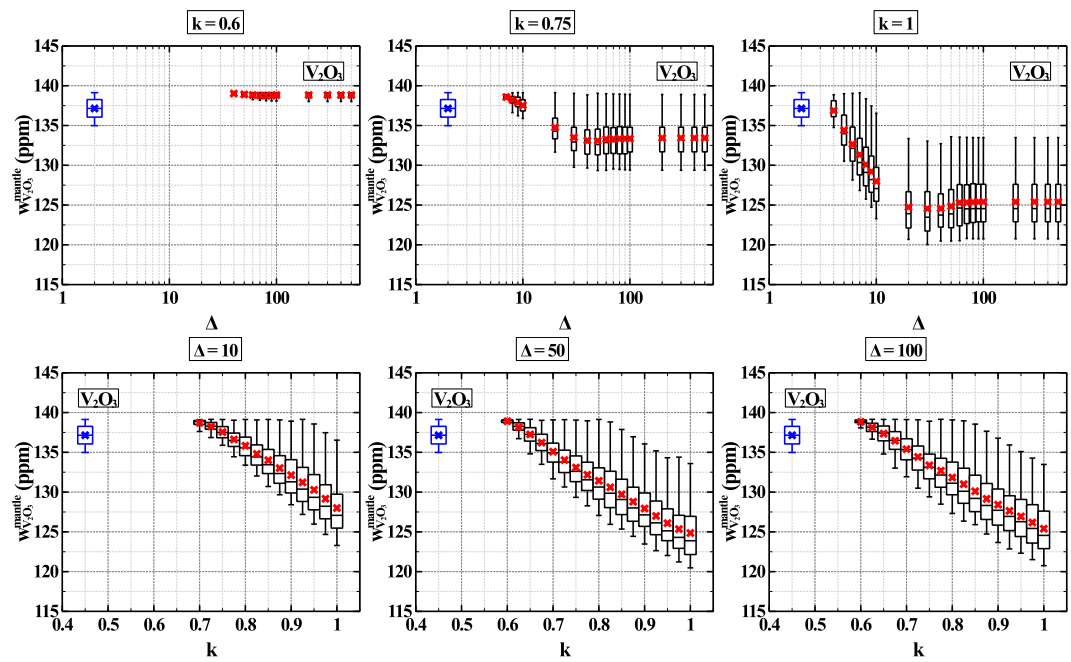


Figure S.12. Evolution of V_2O_3 concentrations (ppm) in the mantle as a function of Δ for fixed values of k (top row), and as a function of k for fixed values of Δ (bottom row). In each panel the entire solutions range are presented as boxplots, with the red cross being the mean value of the parameter, the white box delimiting the 1st and 3rd quartile, the horizontal line the median value and the vertical lines the minimum and maximum values. The reference model dataset is presented in blue with the same type of plot for comparison.

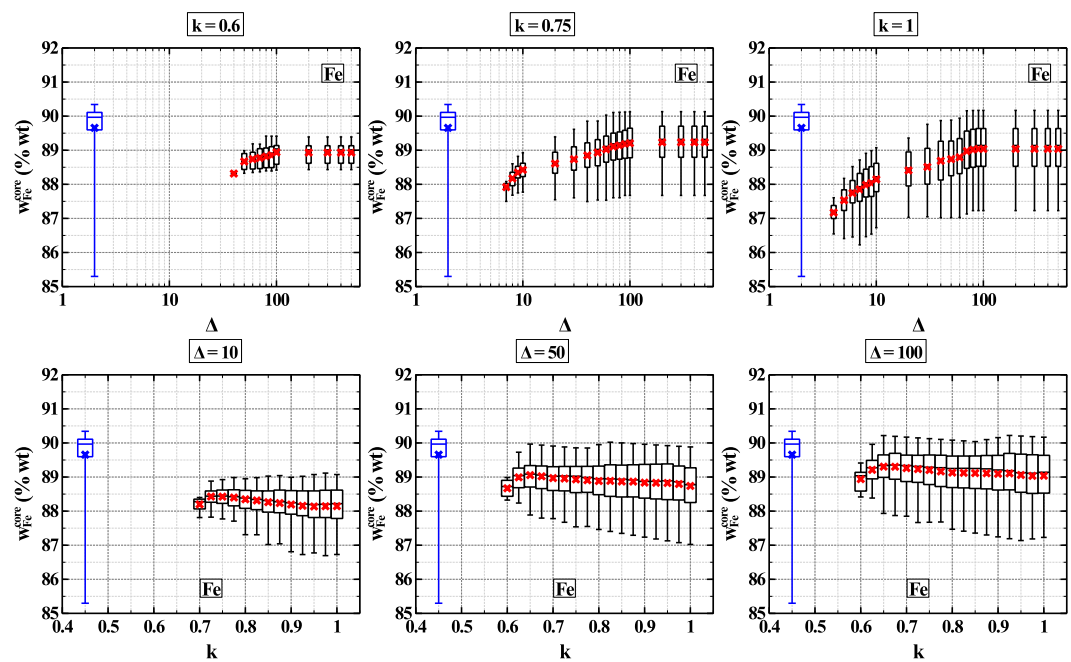


Figure S.13. Evolution of Fe concentrations (% wt) in the core as a function of Δ for fixed values of k (top row), and as a function of k for fixed values of Δ (bottom row). In each panel the entire solutions range are presented as boxplots, with the red cross being the mean value of the parameter, the white box delimiting the 1st and 3rd quartile, the horizontal line the median value and the vertical lines the minimum and maximum values. The reference model dataset is presented in blue with the same type of plot for comparison.

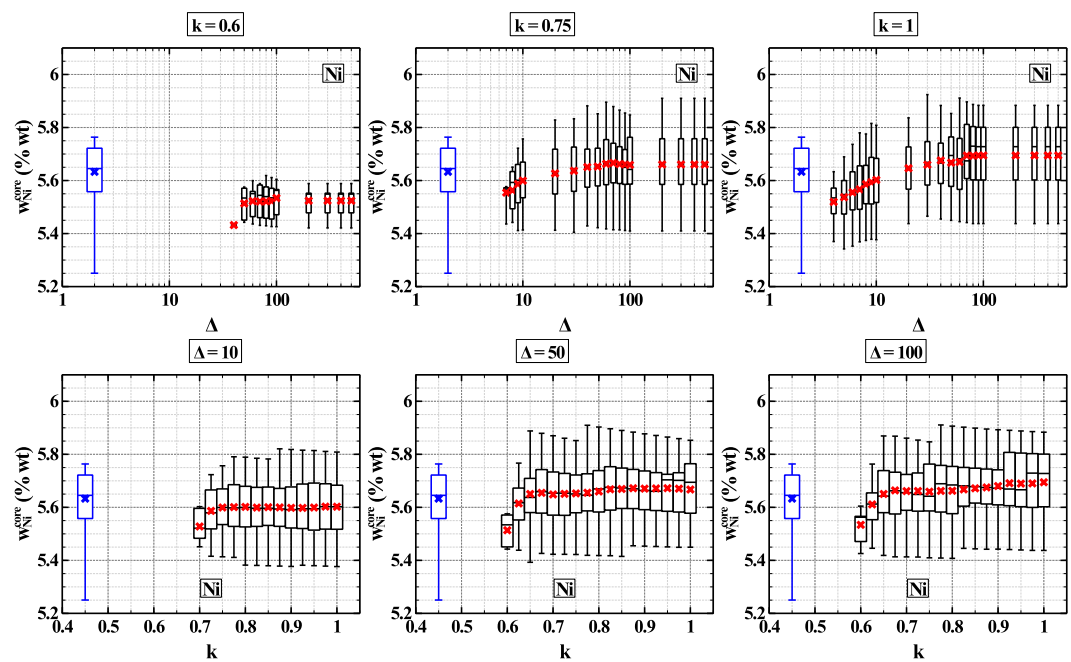


Figure S.14. Evolution of Ni concentrations (% wt) in the core as a function of Δ for fixed values of k (top row), and as a function of k for fixed values of Δ (bottom row). In each panel the entire solutions range are presented as boxplots, with the red cross being the mean value of the parameter, the white box delimiting the 1st and 3rd quartile, the horizontal line the median value and the vertical lines the minimum and maximum values. The reference model dataset is presented in blue with the same type of plot for comparison.

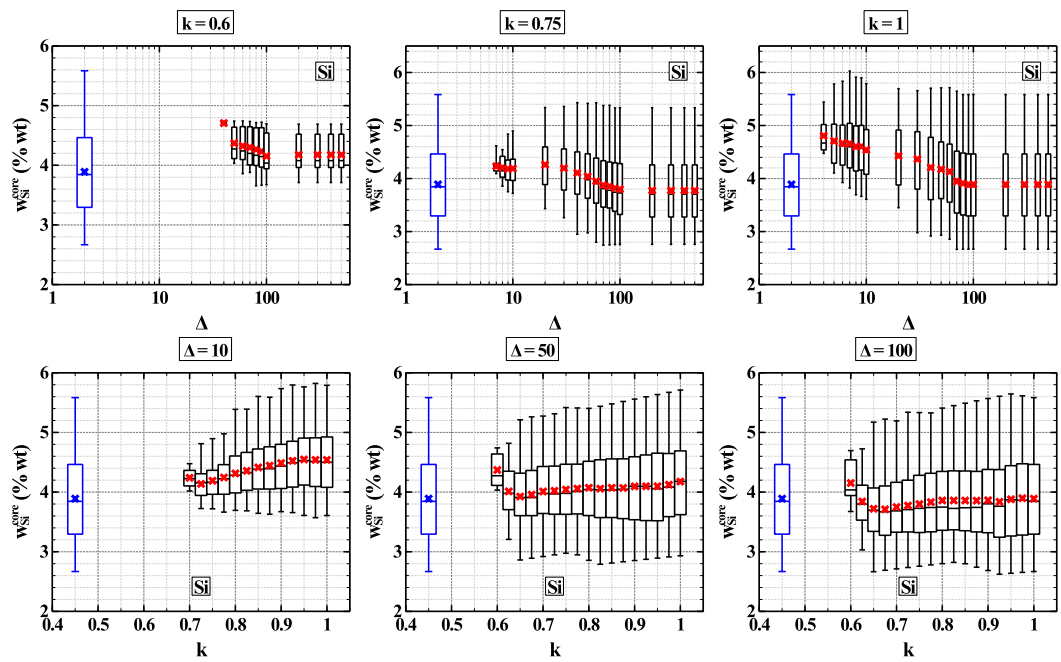


Figure S.15. Evolution of Si concentrations (% wt) in the core as a function of Δ for fixed values of k (top row), and as a function of k for fixed values of Δ (bottom row). In each panel the entire solutions range are presented as boxplots, with the red cross being the mean value of the parameter, the white box delimiting the 1st and 3rd quartile, the horizontal line the median value and the vertical lines the minimum and maximum values. The reference model dataset is presented in blue with the same type of plot for comparison.

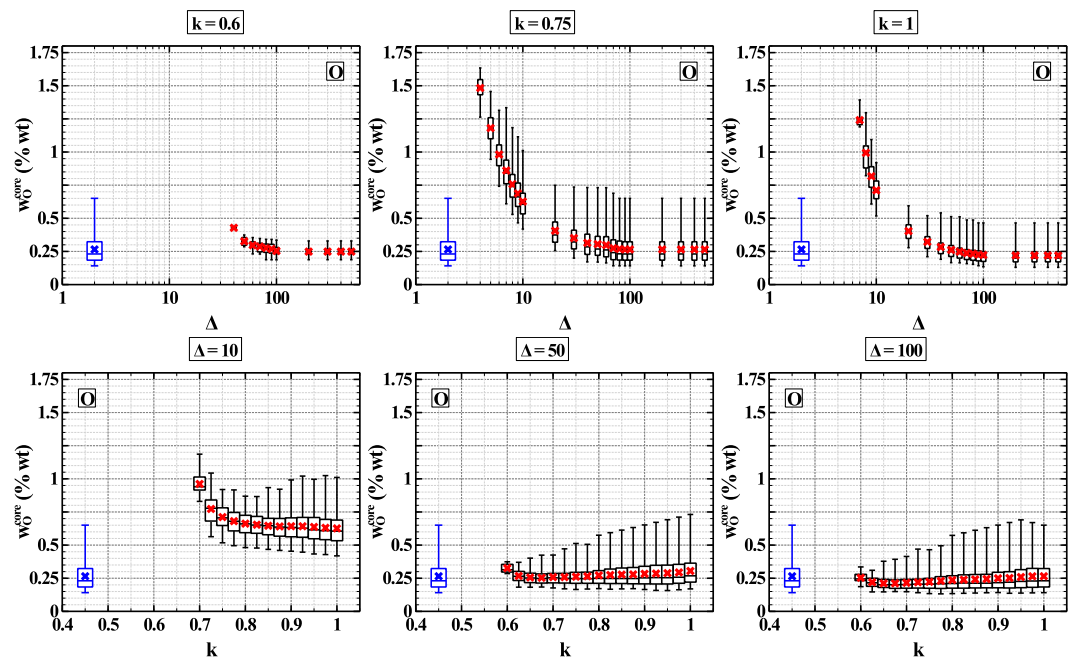


Figure S.16. Evolution of O concentrations (% wt) in the core as a function of Δ for fixed values of k (top row), and as a function of k for fixed values of Δ (bottom row). In each panel the entire solutions range are presented as boxplots, with the red cross being the mean value of the parameter, the white box delimiting the 1st and 3rd quartile, the horizontal line the median value and the vertical lines the minimum and maximum values. The reference model dataset is presented in blue with the same type of plot for comparison.

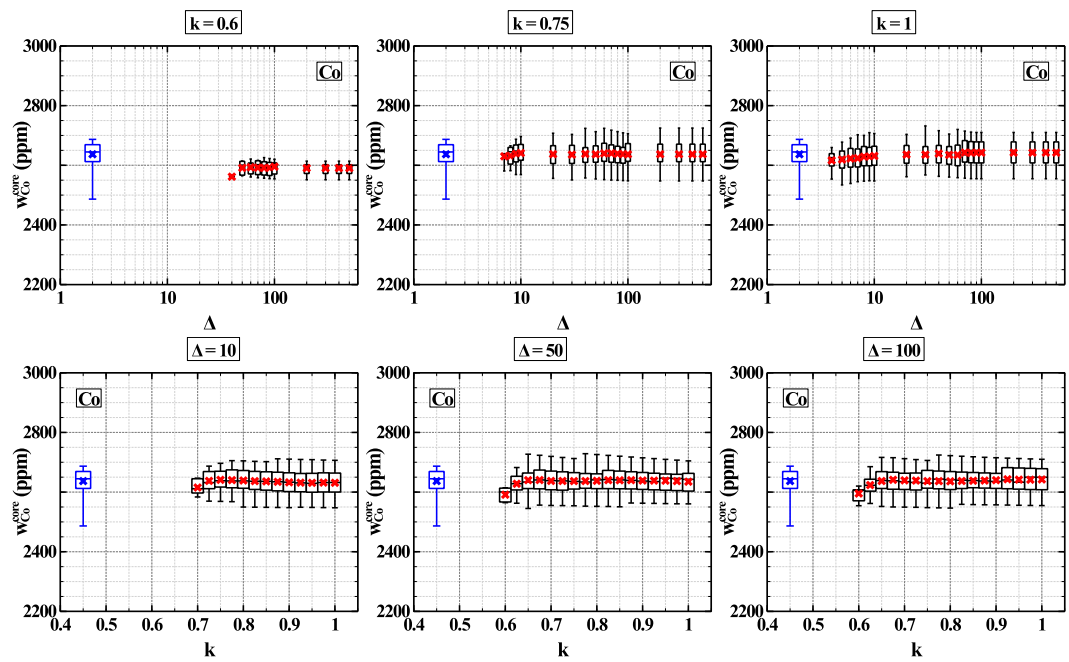


Figure S.17. Evolution of Co concentrations (ppm) in the core as a function of Δ for fixed values of k (top row), and as a function of k for fixed values of Δ (bottom row). In each panel the entire solutions range are presented as boxplots, with the red cross being the mean value of the parameter, the white box delimiting the 1st and 3rd quartile, the horizontal line the median value and the vertical lines the minimum and maximum values. The reference model dataset is presented in blue with the same type of plot for comparison.

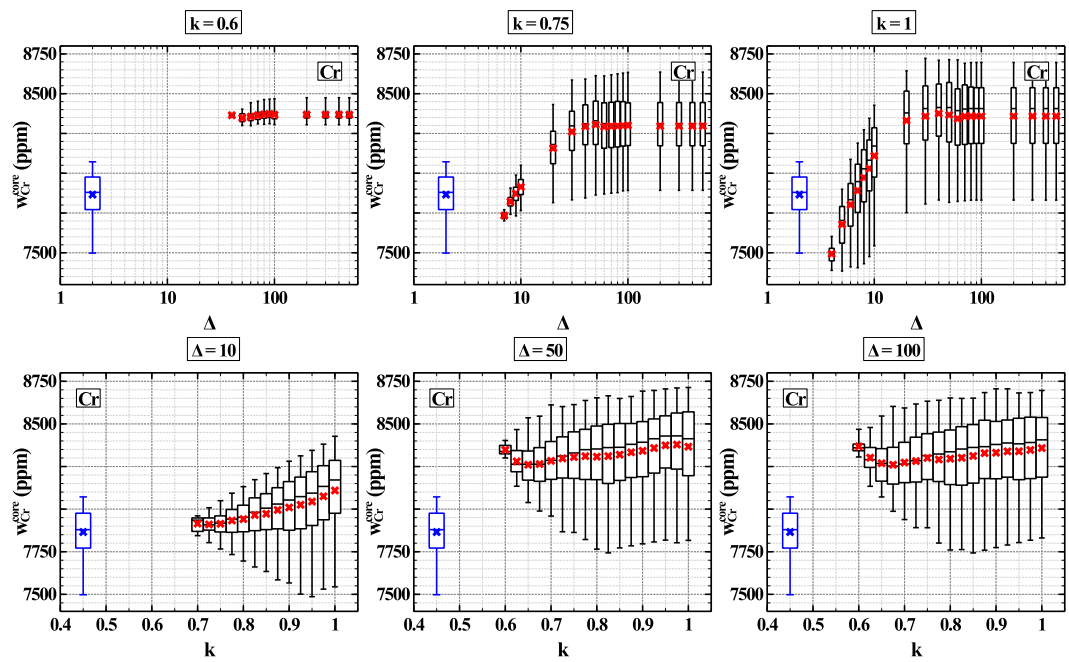


Figure S.18. Evolution of Cr concentrations (ppm) in the core as a function of Δ for fixed values of k (top row), and as a function of k for fixed values of Δ (bottom row). In each panel the entire solutions range are presented as boxplots, with the red cross being the mean value of the parameter, the white box delimiting the 1st and 3rd quartile, the horizontal line the median value and the vertical lines the minimum and maximum values. The reference model dataset is presented in blue with the same type of plot for comparison.

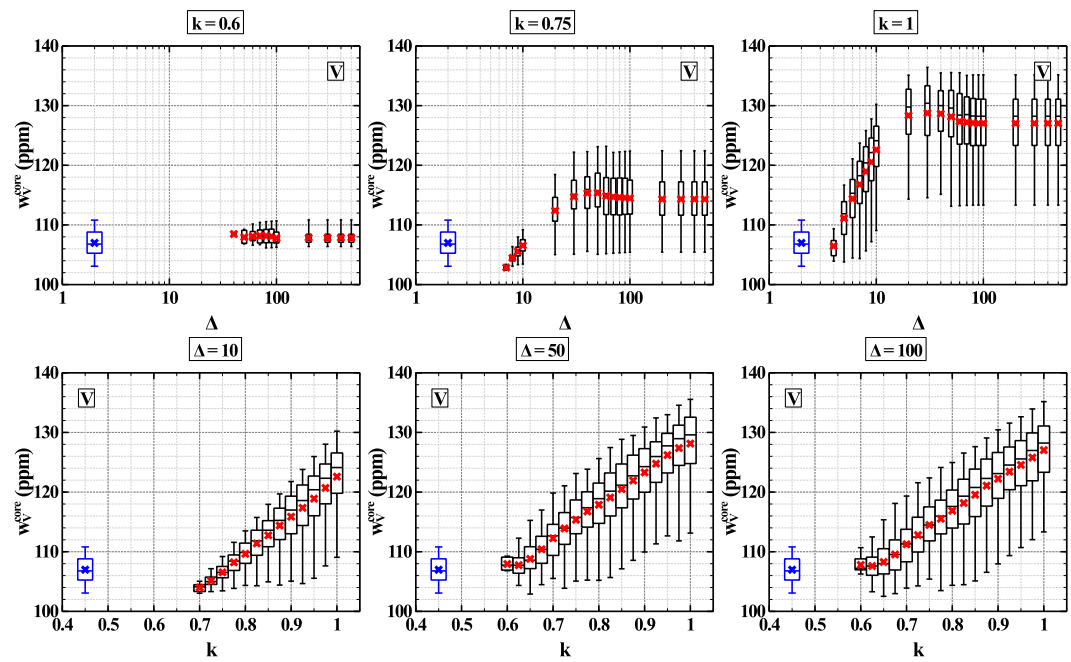


Figure S.19. Evolution of V concentrations (ppm) in the core as a function of Δ for fixed values of k (top row), and as a function of k for fixed values of Δ (bottom row). In each panel the entire solutions range are presented as boxplots, with the red cross being the mean value of the parameter, the white box delimiting the 1st and 3rd quartile, the horizontal line the median value and the vertical lines the minimum and maximum values. The reference model dataset is presented in blue with the same type of plot for comparison.